

# ZIP: Scalable Crowd Counting via Zero-Inflated Poisson Modeling

Yiming Ma<sup>1</sup>, Victor Sanchez<sup>2</sup>, Tanaya Guha<sup>3</sup>

<sup>1</sup>University of Warwick, Coventry CV4 7AL, U.K.

<sup>2</sup>University of Warwick, Coventry CV4 7AL, U.K.

<sup>3</sup>University of Glasgow, Glasgow G12 8RZ, U.K.

yiming.ma.1@warwick.ac.uk, v.f.sanchez-silva@warwick.ac.uk, tanaya.guha@glasgow.ac.uk

## Abstract

Most crowd counting methods directly regress blockwise density maps using Mean Squared Error (MSE) losses. This practice has two key limitations: 1) it fails to account for the extreme spatial sparsity of annotations—over 95% of standard ( $8 \times 8$ ) blocks are empty across most benchmarks, so supervision signals in informative regions are diluted by the predominant zeros; 2) MSE corresponds to a Gaussian error model that poorly matches discrete, non-negative count data. To address these issues, we introduce **ZIP**, a scalable crowd counting framework that models blockwise counts with a **Zero-Inflated Poisson** likelihood: a zero-inflation term learns the probability a block is structurally empty (handling excess zeros), while the Poisson component captures expected counts when people are present (respecting discreteness). We provide a generalization analysis showing a tighter risk bound for ZIP compared to that of MSE-based losses and optimal-transport-based losses, provided that the training resolution is moderately large. To assess the scalability of ZIP, we apply it to backbones spanning over  $100\times$  in parameters/compute. Experiments on ShanghaiTech A & B, UCF-QNRF, and NWPU-Crowd demonstrate that ZIP consistently achieves state-of-the-art performance across all compared model scales. Particularly, on UCF-QNRF, ZIP outperforms mPrompt by almost 3 MAE and 12 RMSE, demonstrating its effectiveness even in extremely dense crowd scenes.

## Introduction

Crowd counting aims to estimate the number of people present in an image or a video frame. It has a broad range of real-world applications, including public safety and crowd management (Valencia et al. 2021), and intelligent transportation systems (McCarthy et al. 2025). The majority of existing crowd counting methods (Ma et al. 2019; Cheng et al. 2022; Han et al. 2023; Ranasinghe et al. 2024) construct blockwise training targets by first convolving point annotations with Gaussian kernels to create a pixel-level density map, and then summing density values within each  $8 \times 8$  block to obtain blockwise density maps. Models are trained to regress these blockwise targets (usually with Mean Squared Error (MSE)) in lieu of raw pixel supervision to mitigate extreme pixel-level sparsity.

In the above methods, however, the aggregated blockwise density maps remain **highly sparse**: across ShanghaiTech A & B (Zhang et al. 2016), UCF-QNRF (Idrees

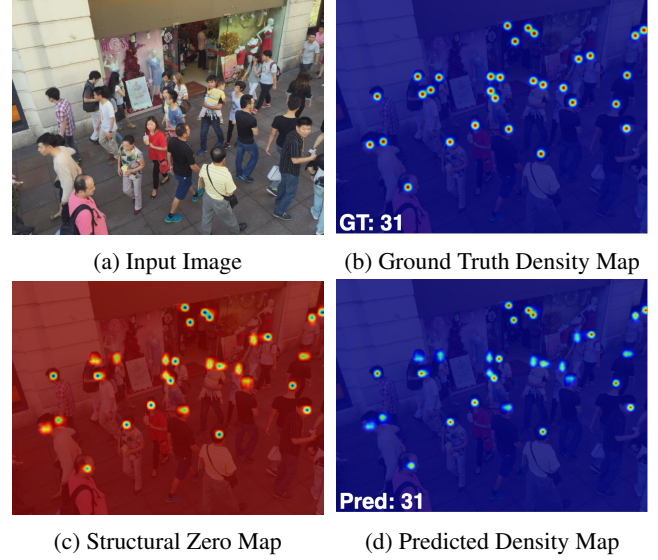


Figure 1: The structural zero map output by ZIP can accurately segment non-head-central regions, thereby highlighting only candidate head-center areas. This visualization uses an image from the ShanghaiTech B test split. **Color scale (all panels):** red = higher value, blue = lower value (per-panel normalization). In (c), red regions have *high* probability of being structurally empty (background, torso, peripheral head parts), blue indicates *low* structural-zero probability (*i.e.*, candidate head centers). In (d), red regions correspond to *high* expected local crowd density near head centers; blue denotes near-zero density. This structural-zero modeling addresses density map sparsity by masking out semantically empty regions.

et al. 2018), and NWPU-Crowd (Wang et al. 2020c), over 95% of  $8 \times 8$  blocks contain zero people (empirical measurement). This zero dominance skews squared-error losses, dilutes supervision from populated regions, and biases models toward under-counting. These methods also suffer from **label noise** introduced by Gaussian smoothing. Point annotations are spatially uncertain: a human click marks an approximate head center, and nearby pixels could be equally valid. Spreading each point with a local kernel is intended to

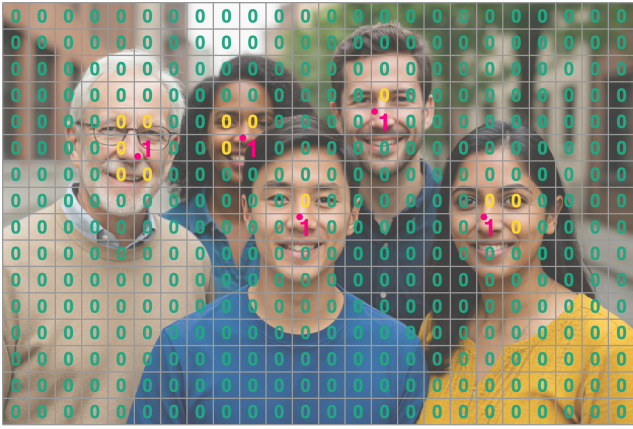


Figure 2: Illustration of the concept of structural and sampling zeros in ZIP (best viewed in color). The image (synthesized for illustration purposes) is overlaid with a grid where each cell represents a spatial block. The red dot marks a ground-truth head annotation, and the block containing it is labeled with the red number “1”. Yellow zeros, which indicate sampling zeros, are assigned to blocks that correspond to the head-center region but receive zero count due to the point-based annotation protocol. Green zeros denote structural zeros, corresponding to background regions, non-head body parts or outer regions of the head that are not associated with any annotations.

make supervision tolerant to such subjective variation. However, since the true head extents are unknown, mismatched kernel bandwidths yield over- or under-counts after block aggregation and thus inject noise into learning targets.

Prior work attempts to mitigate sparsity by first segmenting foreground crowd regions and then counting only within those areas (Rong and Li 2021; Modolo et al. 2021; Guo et al. 2024). Such a practice introduces additional multi-task loss balancing complexity. Also, since crowd counting datasets are not annotated with segmentation masks, these approaches usually derive pseudo masks from Gaussian-smoothed density maps, inheriting the same head-size uncertainty and label noise discussed above.

In addition, MSE-based loss functions present a **modeling mismatch**. Blockwise targets represent discrete, non-negative, and zero-heavy count data, whereas MSE implicitly assumes Gaussian residuals on continuous values. A Poisson model can capture both the discreteness and non-negativity of counts, yet a standard Poisson struggles with the overwhelming presence of zeros. These gaps motivate a formulation that explicitly separates structural emptiness from stochastic counts, leading to our Zero-Inflated Poisson (ZIP) framework.

Our ZIP framework hypothesizes that zeros in blockwise density maps arise from two distinct mechanisms :

- **Structural zeros**, which are blocks that are deterministically zero due to their semantic irrelevance. These include background (sky, buildings, etc.), body parts (limbs, chest, etc.) and peripheral head regions that do

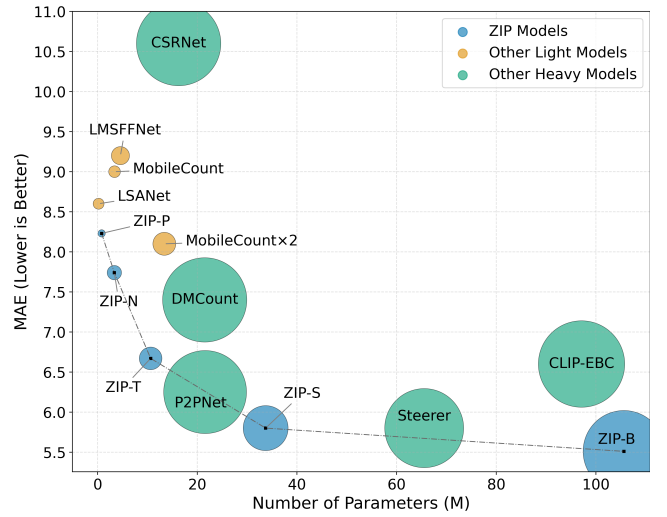


Figure 3: Scalability of the proposed ZIP framework on ShanghaiTech B. Each circle represents a specific model, where the radius corresponds to the number of floating point operations (FLOPs) required to process a single  $1920 \times 1080$  image during inference. ZIP models (in blue) exhibit a favorable trade-off between model size and accuracy, demonstrating better scalability compared to other lightweight (yellow) and heavyweight (green) models.

not correspond to head centers, and they comprise the majority of zero blocks. Fig. 1c illustrates this type of zeros predicted by ZIP on ShanghaiTech B.

- **Sampling zeros**: each head is annotated by a *single point* which is assigned to a unique supervision block. Neighboring blocks that also correspond to the head center therefore receive zero count. Modeling these annotation effects in the Poisson component absorbs the positional ambiguity that Gaussian smoothing is meant to solve, removing kernel bandwidth tuning.

Fig. 2 provides a schematic comparison of these two types of zeros. Because structural and sampling zeros are not annotated separately, our ZIP model learns to distinguish these two types of zeros implicitly by optimizing the negative log-likelihood of the ZIP distribution, with the Poisson rate additionally supervised by a cross entropy loss to stabilize training. Empirically, learned zero-inflation correlates with non-head-center areas. As illustrated in Fig. 1, the structural-zero map in 1c predicts nearly all non-head pixels as zeros, while preserving only the compact blue blobs centered on heads. Compared with segmentation-based methods, our ZIP-based method offers several notable advantages: 1) it does not rely on segmentation masks, thereby avoiding noise introduced by Gaussian smoothing; 2) it captures structural sparsity without assuming the presence of clear object boundaries, making it better suited for highly occluded and densely crowded scenes; 3) it eliminates the need to balance counting and segmentation, simplifying the training objective.

Through theoretical risk bound analysis (see Theorem 1)



and comprehensive empirical evaluation, we show that ZIP consistently outperforms Gaussian-smoothed MSE-based losses and DMCount (Wang et al. 2020a). To further assess the scalability of ZIP, we evaluate its performance with backbones of varying computational complexities, including MobileNet, MobileCLIP, and CLIP-ConvNeXt. As illustrated in Fig. 3, our ZIP framework consistently outperforms existing models in both accuracy (measured by Mean Absolute Error (MAE)) and computational efficiency (measured by FLOPs) across different parameter scales, demonstrating its superior scalability. To summarize, our contributions are:

- We propose a novel crowd counting framework **ZIP** based on **Zero-Inflated Poisson (ZIP)** regression, which explicitly models the extreme sparsity of ground-truth count distributions by disentangling structural zeros from sampling uncertainty.
- We present both **theoretical risk bound analysis** and thorough **experiments on four crowd counting benchmarks** to validate the effectiveness of our ZIP framework. Results show that our base model, **ZIP-Base**, consistently outperforms existing state-of-the-art methods across four different datasets.
- We present a systematic study of **framework-level scalability** in crowd counting. Our ZIP framework generalizes well across a wide range of model sizes and architectures, from lightweight convolutional neural networks (CNNs) to vision-language models, achieving state-of-the-art performance under varying computational constraints.

## Related Work

To address the extreme sparsity of ground-truth density maps, many existing methods (Zhang et al. 2016; Liu, Salzmann, and Fua 2019; Ma et al. 2019; Wang et al. 2020b, 2021; Han et al. 2023; Guo et al. 2024) adopt Gaussian smoothing. These approaches typically preprocess the ground-truth density map by convolving it with Gaussian kernels, either of fixed or adaptive size. In principle, the kernel size should reflect the actual head size in the image; however, such information is typically unavailable in most crowd counting datasets. As a result, Gaussian smoothing inevitably introduces noise into the ground-truth density maps, which can degrade the model’s generalization ability (Wang et al. 2020a). There have also been some efforts (Rong and Li 2021; Modolo et al. 2021; Guo et al. 2024) to address the sparsity by training a segmentation model which aims to separate regions containing people from the background. However, most crowd counting datasets do not provide segmentation masks, they have to rely on Gaussian-smoothed ground-truth density maps to generate pseudo ground-truth segmentation masks. This again introduces noise into the pseudo segmentation masks. Guo et al. exploited the box annotations provided by NWPU-Crowd (Wang et al. 2020c) to handle this problem, but compared with point annotations, box annotations are much more expensive to acquire. Besides, these methods introduce an extra task to counting, and how to balance the loss terms in such a multi-task setting poses a new challenge.

On the other hand, most density-based crowd counting methods typically frame the task as a regression problem, where the model is trained to minimize the blockwise mean squared error (MSE) between the predicted and ground-truth blockwise density maps (Zhang et al. 2016; Liu, Salzmann, and Fua 2019; Liu et al. 2019; Ma et al. 2019; Wang et al. 2020b; Han et al. 2023; Guo et al. 2024). This loss function implicitly assumes that each blockwise count follows a Gaussian distribution centered at the predicted value. This formulation fails to capture the discreteness and non-negativity of count data. DMCount (Wang et al. 2020a) addresses a different issue by reformulating density estimation as an Earth Mover’s Distance (EMD) problem. By minimizing the Wasserstein distance between predicted and ground-truth density maps, DMCount explicitly models the global transportation cost needed to match the predicted mass to the annotated points. Similar to MSE-based methods, it still operates entirely in a continuous density space, treating the density maps as divisible mass rather than integer-valued counts. Also, the exact computation of EMD scales poorly with the number of bins ( $\mathcal{O}(n^3)$ ).

## Method

In this work, we propose to incorporate **Zero-Inflated Poisson (ZIP)** regression to address the extreme sparsity of ground-truth density maps. Our ZIP framework bypasses Gaussian smoothing and models per-block counts  $y \in \mathbb{N}$  via a zero-inflated Poisson :

$$P(y = k | \pi, \lambda) = \begin{cases} \pi + (1 - \pi)e^{-\lambda}, & k = 0 \\ (1 - \pi) \frac{e^{-\lambda} \lambda^k}{k!}, & k > 0 \end{cases} \quad (1)$$

with  $\pi, \lambda$  predicted per block. Fig. 4 illustrates an overview of the proposed ZIP framework.

### Zero-Inflated Poisson Regression

Since training crowd counting models directly via regression can suffer from unstable gradient updated, we follow the Enhanced Block Classification (EBC) framework (Ma, Sanchez, and Guha 2024) to first quantize blockwise counts into integer-valued bins  $\{\mathcal{B}_k\}_{k=1}^n$  with bin centers  $\{b_k\}_{k=1}^n$ .

Given an input image  $\mathbf{X} \in \mathbb{R}^{3 \times H \times W}$ , we first compute the feature map  $\mathbf{f}$  using a shared backbone:

$$\mathbf{f} = \mathbf{F}(\mathbf{X}) \in \mathbb{R}^{C \times h \times w} \quad (2)$$

where  $h = H/r$ ,  $w = W/r$  denote the spatial size of the output, and  $r$  represents the block size.

Then, the feature map  $\mathbf{f}$  is passed through a  $\lambda$ -head  $H_\lambda$  (implemented as a  $1 \times 1$  convolution), followed by a softmax activation to generate a probability distribution over the  $n-1$  positive count bins:

$$P_\lambda^* = \text{Softmax}(H_\lambda(\mathbf{f})) \in \mathbb{R}^{(n-1) \times h \times w}. \quad (3)$$

Note that we exclude the  $\mathcal{B}_1 = \{0\}$  bin here, since the Poisson distribution assumes a strictly positive rate  $\lambda > 0$ . We then compute the estimated Poisson rate map  $\lambda \in \mathbb{R}_+^{1 \times h \times w}$  as the expected value of the bin centers:

$$\lambda_{i,j} = \sum_{k=2}^n P_{\lambda_{k,i,j}}^* \cdot b_k, \quad (4)$$

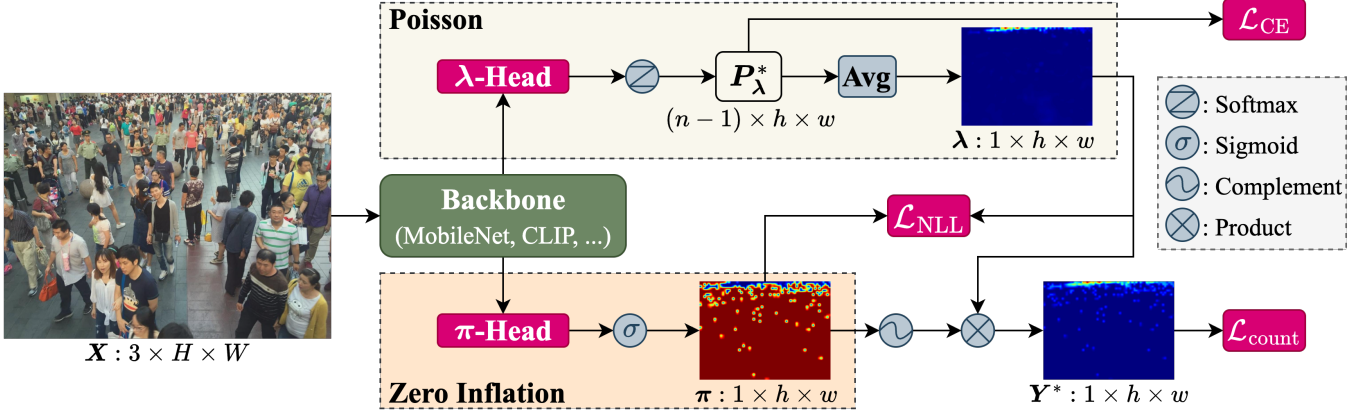


Figure 4: Overview of the proposed ZIP framework. Given an input image  $X$  of spatial size  $H \times W$ , a backbone network extracts feature maps that are shared by two parallel branches: A Poisson branch (top) and a Zero Inflation branch (bottom). The Poisson branch (top) processes the features through a  $\lambda$ -head with a softmax activation, producing the blockwise count distribution  $P_\lambda^*$  over  $(n-1)$  positive bins. The Poisson rate per block is computed as a weighted average of bin centers, yielding the final  $\lambda$  map. In the Zero Inflation branch, the same features are fed to a  $\pi$ -head with a sigmoid activation to estimate the structural zero probability map  $\pi$  of spatial size  $h \times w$ . The predicted density map  $Y^*$  is defined as the expected value of the zero-inflated Poisson distribution:  $Y^* = (1 - \pi) \otimes \lambda$ , where  $\otimes$  denotes elementwise multiplication.

where  $b_k$  for  $k = 2, \dots, n$  denotes the center of each positive bin.

The learning of  $P_\lambda^*$  is supervised by a cross-entropy loss over the positive regions of the ground-truth density map. Specifically, we define the set of positive-valued blocks as  $Y_+ := Y[Y > 0]$ , which arise from the Poisson component and are thus only related to  $\lambda$ . Their corresponding probabilistic predictions  $P_{\lambda+}^*$  can be obtained via  $P_{\lambda+}^* = P_\lambda^*[Y > 0]$ . The cross-entropy loss is calculated based on  $P_{\lambda+}^*$  and  $Y_+$ :

$$\mathcal{L}_{CE} = \text{CrossEntropy}(P_{\lambda+}^*, P_+), \quad (5)$$

where  $P_+$  is the one-hot encoded ground-truth probability map of  $Y_+$ .

In parallel, we introduce a  $\pi$ -head,  $H_\pi$ , also implemented as a  $1 \times 1$  convolution, followed by a sigmoid activation to produce the structural zero probability map:

$$\pi = \sigma(H_\pi(f)) \in \mathbb{R}^{1 \times h \times w} \quad (6)$$

The negative log-likelihood (NLL) loss of the zero-inflated Poisson distribution is given by:

$$\mathcal{L}_{NLL} = -\frac{1}{hw} \sum_{i=1}^h \sum_{j=1}^w \log P(Y_{i,j} | \pi_{i,j}, \lambda_{i,j}) \quad (7)$$

where  $P(Y_{i,j} | \pi_{i,j}, \lambda_{i,j})$  is the p.m.f. of the ZIP distribution given by Eq. (1), and  $\lambda$  and  $\pi$  are given by (4) and (6), respectively.

It is important to note that we do not supervise the  $\pi$  and  $\lambda$  branches separately. Since structural and sampling zeros are not explicitly annotated in the ground-truth, we treat them as latent factors and optimize both branches jointly via the ZIP negative log-likelihood loss in Eq. (7). This formulation allows the model to implicitly learn to disentangle the two

types of zeros based on the statistical patterns in the data, without requiring additional annotations.

We use the expectation map  $Y^* = \mathbb{E}[Y | \pi, \lambda]$  as the predicted density map, given by

$$Y^* = (1 - \pi) \otimes \lambda \in \mathbb{R}^{1 \times h \times w} \quad (8)$$

where  $\otimes$  represents element-wise multiplication.

To ensure accurate crowd estimates at the image level, we incorporate a count loss that penalizes discrepancies between the predicted and ground-truth total counts. The predicted total count  $c^*$  is obtained by summing over all elements of the predicted density map:

$$c^* = \sum_{i=1}^h \sum_{j=1}^w Y_{i,j}^*. \quad (9)$$

We define the count loss as the MAE between the predicted and ground-truth total counts:

$$\mathcal{L}_{count} = |c^* - c| = \left| \sum_{i=1}^h \sum_{j=1}^w (Y_{i,j}^* - Y_{i,j}) \right| \quad (10)$$

Finally, the model is trained using a weighted sum of three loss terms:

$$\mathcal{L}_{total} = \omega \mathcal{L}_{CE} + \mathcal{L}_{NLL} + \mathcal{L}_{count}, \quad (11)$$

where  $\omega$  is a scalar weighting coefficients, and  $\mathcal{L}_{CE}$ ,  $\mathcal{L}_{NLL}$ , and  $\mathcal{L}_{count}$  are defined in Eq. (5), (7), and (10), respectively.

### ZIP has a Tighter Risk Bound

Since Wang et al. established that DMCount enjoys a tighter risk bound than Gaussian-smoothed MSE-based losses, it suffices for us to show that the ZIP NLL loss defined in Eq. (7) admits an even tighter risk bound than DMCount. We formalize this result in the following theorem.

Suffix	Backbone	Size (M)	FLOPS (G)
-P (Pico)	MobileNetV4-Small-0.5×	0.81	6.46
-N (Nano)	MobileNetV4-Small	3.36	24.73
-T (Tiny)	MobileNetV4-Medium	10.64	61.62
-S (Small)	MobileCLIP-S1	33.72	242.68
-B (Base)	CLIP-ConvNeXt-Base	105.60	800.99

Table 1: ZIP variants with corresponding backbones, parameter sizes, and computational complexity measured on a  $1920 \times 1080$  resolution.

**Theorem 1.** Assume that the per-block counts follow a zero-inflated Poisson (ZIP) distribution parameterized by block-wise parameters  $\theta = (\pi, \lambda)$ , with  $\pi > 0$ . Let  $\mathcal{H}$  denote the hypothesis class of scalar regressors (e.g., the shared backbone and prediction heads), and define the full hypothesis class as the blockwise product  $\mathcal{F} := \mathcal{H}^{\times hw}$ , where  $hw$  is the total number of spatial blocks. Let  $f_S^{\text{NLL}}$  be the empirical risk minimizer of the ZIP negative log-likelihood loss  $\mathcal{L}_{\text{NLL}}$  over the sample  $\mathcal{S}$ , and let  $f_D^{\text{NLL}}$  be the population minimizer of the same loss. Then, for any  $\delta \in (0, 1)$ , with probability at least  $1 - \delta$  over the random draw of  $\mathcal{S}$ , the following generalization bound holds:

$$\begin{aligned} \mathcal{R}_D(f_S^{\text{NLL}}, \mathcal{L}_{\text{NLL}}) - \mathcal{R}_D(f_D^{\text{NLL}}, \mathcal{L}_{\text{NLL}}) \\ \leq 2 \cdot hw \cdot L \cdot R_S(\mathcal{H}) + \mathcal{O}(\sqrt{1/K}), \end{aligned} \quad (12)$$

where  $L$  is the Lipschitz constant of the full-image ZIP loss (per Lemma 2 in the supplementary material), and  $R_S(\mathcal{H})$  is the empirical Rademacher complexity of the base hypothesis class  $\mathcal{H}$ .

By comparison, generalization gap of the OT loss in DM-Count (Wang et al. 2020a) is bounded by

$$\begin{aligned} \mathcal{R}_D(f_S^{\text{OT}}, \mathcal{L}_{\text{OT}}) - \mathcal{R}_D(f_D^{\text{OT}}, \mathcal{L}_{\text{OT}}) \\ \leq 4 \cdot (hw)^2 \cdot C_\infty \cdot R_S(\mathcal{H}) + \mathcal{O}(\sqrt{1/K}). \end{aligned} \quad (13)$$

where  $C_\infty$  is the maximum cost in the cost matrix in OT. Hence, when  $h$  or  $w$  grows, the upper bound of ZIP (Eq. (12)) becomes tighter than that of OT (Eq. (13)). The proof of Theorem 1 and the risk bound of the overall loss function Eq. (11) can be found in the supplementary material.

## Experiments

**Variants.** To evaluate the scalability and adaptability of our proposed framework, we construct five model variants of ZIP with different backbones, including MobileNetV4 (Qin et al. 2024), MobileCLIP (Vasu et al. 2024) and OpenCLIP’s ConvNeXt-Base (Liu et al. 2022; Cherti et al. 2023). These variants are suitable for different application scenarios, ranging from mobile-friendly to high-performance settings. The specifications are summarized in Table 1. All variants share the same head design and differ only in backbone complexity. This modularity allows ZIP to scale across computational budgets.

**Setup.** Our training configuration largely follows EBC. We first preprocess all datasets so that the minimum edge length

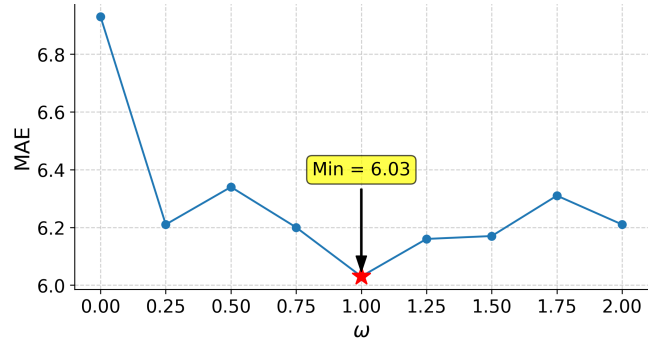


Figure 5: Performance of the VGG19-based structure on ShanghaiTech B under varying values of  $\omega$  in Eq. (11). Results indicate that  $\omega = 1.00$  gives the lowest MAE (6.03).

Loss Function Component	MAE	RMSE	NAE
MAE	6.39	10.66	5.34%
MSE	6.90	11.41	5.30%
DMCount (Wang et al. 2020a)	6.62	11.35	5.30%
Poisson NLL	6.21	10.25	5.02%
ZIP NLL (ours)	<b>6.03</b>	<b>9.95</b>	<b>4.99%</b>

Table 2: Ablation study on the proposed ZIP NLL loss in Eq. (7). We replace it with alternative choices in the total loss function in Eq. (11) on ShanghaiTech B, while  $\mathcal{L}_{\text{CE}}$  and  $\mathcal{L}_{\text{count}}$  remain unchanged. Results show that our ZIP NLL achieves the lowest MAE, RMSE, and NAE.

is no less than 448. We limit the maximum edge length of UCF-QNRF to be 2048 and that of NWPU-Crowd to be 3072. We apply a combination of data augmentation techniques, including random resized cropping, horizontal flipping, and color jittering (see supplementary material for more details). Block sizes are set to 16 for ShanghaiTech A & B and NWPU-Crowd, and 32 for UCF-QNRF. All models are optimized using the Adam optimizer with a weight decay of  $1e - 4$ . The learning rate is linearly warmed up from  $1e - 5$  to  $1e - 4$  over the first 25 epochs, followed by cosine annealing with parameters  $T_0 = 5$  and  $T_{\text{mult}} = 2$ . To determine the optimal results, all experiments were conducted for 1,300 epochs using the PyTorch framework (v2.7.1).

**Evaluation metrics.** Following standard practice, we evaluate each model variant on all datasets using three commonly adopted metrics: MAE, RMSE, and Normalized Absolute Error (NAE). The NAE metric ensures fair evaluation across both sparse and dense scenes by normalizing the absolute error with respect to the ground-truth count.

## Ablation Study

We first determine the optimal value of the weighting parameter  $\omega$  in Eq.(11), which balances the cross-entropy term and other two terms. To this end, we evaluate the VGG19-based encoder-decoder model under various settings of  $\omega$  on the ShanghaiTech B dataset and report the results in Fig. 5. As illustrated, the model achieves the lowest MAE (6.03) when  $\omega = 1.00$ , and thus, we fix  $\omega = 1.00$  at this value for all



Method	ShanghaiTech A		ShanghaiTech B		UCF-QNRF		NWPU (Val)	
	MAE	RMSE	MAE	RMSE	MAE	RMSE	MAE	RMSE
ChfL (Shu et al. 2022)	57.5	94.3	6.9	11.0	80.3	137.6	76.8	343.0
MAN (Lin et al. 2022)	56.8	90.3	-	-	77.3	131.5	76.5	323.0
CLTR (Liang, Xu, and Bai 2022)	56.9	95.2	6.5	10.6	85.8	141.3	61.9	246.3
CrowdHat (Wu and Yang 2023)	51.2	81.9	5.7	9.4	75.1	<u>126.7</u>	-	-
STEERER (Han et al. 2023)	54.5	86.9	5.8	8.5	74.3	128.3	54.3	238.3
PET (Liu et al. 2023)	49.3	78.8	6.2	9.7	79.5	144.3	58.5	238.0
APGCC (Chen et al. 2024)	<u>48.8</u>	<u>76.7</u>	<u>5.6</u>	<u>8.7</u>	80.1	133.6	-	-
Gramformer (Lin et al. 2024)	54.7	87.1	-	-	76.7	129.5	-	-
mPrompt (Guo et al. 2024)	52.5	88.9	5.8	9.6	<u>72.2</u>	133.1	50.2	219.0
CLIP-EBC (Ma, Sanchez, and Guha 2024)	52.5	83.2	6.0	10.1	80.3	136.6	<u>36.6</u>	<u>81.7</u>
<b>ZIP-B (ours)</b>	<b>47.8</b>	<b>75.0</b>	<b>5.5</b>	<b>8.6</b>	<b>69.4</b>	<b>121.8</b>	<b>28.2</b>	<b>64.8</b>

Table 3: Comparison of our model ZIP-B with state-of-the-art models of similar sizes on ShanghaiTech A & B, UCF-QNRF, and the NWPU-Crowd validation split. ZIP-B achieves the best performance across all these four datasets under both MAE and RMSE, surpassing all strong baselines.

subsequent experiments.

To validate the effectiveness of the proposed ZIP NLL loss, we conduct an ablation study where we replace the ZIP NLL component in the total loss function in Eq. (11) with several commonly used alternatives, including MAE, MSE, DMCount (Wang et al. 2020a), and Poisson NLL. Other components in the loss function, such as the cross-entropy loss and the count loss, are kept unchanged. All models are trained using the same VGG19-based architecture under identical settings. The evaluation results on ShanghaiTech B are presented in Table 2. As shown, our ZIP NLL achieves the lowest MAE (6.03), RMSE (9.95) and NAE (4.99%), demonstrating its effectiveness in enhancing counting accuracy while maintaining robust distribution modeling.

### ZIP-B Compared with State-of-the-Art

We first compare our base model, **ZIP-B**, with state-of-the-art crowd counting methods of comparable parameter sizes on four benchmark datasets: ShanghaiTech A & B, UCF-QNRF, and the validation split of NWPU-Crowd. The results are summarized in Table 3. Our method consistently achieves the best performance across all datasets. In particular, on **ShanghaiTech A**, our model achieves the lowest MAE (**47.8**) and RMSE (**75.0**), outperforming the previous best result (48.8 MAE, 76.7 RMSE by APGCC). On **ShanghaiTech B**, we also achieve the best performance with an MAE of **5.5** and an RMSE of **8.6**, significantly surpassing strong baselines such as CrowdHat and STEERER. For the challenging **UCF-QNRF** dataset, our method sets a new state-of-the-art with **69.4** MAE and **121.8** RMSE. On **NWPU-Crowd (val)**, we obtain a substantial improvement over prior methods, achieving **28.2** MAE and **64.8** RMSE, significantly outperforming the closest competitor, CLIP-EBC, which reports 36.6 MAE and 81.7 RMSE.

We further evaluate our method on the NWPU-Crowd test set, with results summarized in Table 4. ZIP-B achieves the lowest MAE (**60.1**) and lowest NAE (**0.104**). Compared to the previous best-performing models, MAE is reduced by

Method	MAE	RMSE	NAE
ChfL (Shu et al. 2022)	76.8	343.0	0.171
MAN (Lin et al. 2022)	76.5	323.0	0.170
CLTR (Liang, Xu, and Bai 2022)	74.4	333.8	0.165
CrowdHat (Wu and Yang 2023)	68.7	296.9	0.181
STEERER (Han et al. 2023)	63.7	309.8	<u>0.133</u>
PET (Liu et al. 2023)	74.4	328.5	-
APGCC (Chen et al. 2024)	71.7	<u>284.4</u>	0.215
Gramformer (Lin et al. 2024)	72.5	316.4	0.160
mPrompt (Guo et al. 2024)	62.1	293.5	-
CLIP-EBC (Ma, Sanchez, and Guha 2024)	<u>61.3</u>	<b>278.4</b>	0.148
<b>ZIP-B (ours)</b>	<b>60.1</b>	299.0	<b>0.104</b>

Table 4: Comparison of our method ZIP-B with the latest approaches of comparable scales on the test split of NWPU-Crowd. ZIP-B achieves both the lowest MAE and NAE, reducing NAE by 21.8% compared to the previous best (STEERER).

1.2 (from 61.3 by CLIP-EBC), and NAE is improved by 21.8% relative to STEERER (from 0.133 to 0.104). While the RMSE (299.0) is not the lowest among all methods, it remains competitive. Given that RMSE is highly sensitive to annotation noise (as illustrated in the supplementary material), MAE and NAE serve as more stable and representative metrics. These results highlight the effectiveness and robustness of ZIP-B across varying crowd densities. We also provide comparisons of ZIP-B with other models under varying illuminance and crowd sizes on NWPU-Crowd in the supplementary material.

### Comparison with Lightweight Models

To investigate the performance-efficiency trade-off, we compare our proposed lightweight models (from ZIP-P to ZIP-S) with a range of representative compact methods. We divide models into four groups based on parameter size: (1) ultra-lightweight models (<1M), (2) lightweight models (1–10M), (3) mid-size models (10–20M), and (4) larger lightweight models ( $\geq 20$ M). Table 5 presents the details.

Method	Size (M)	FLOPS (G)	ShanghaiTech A		ShanghaiTech B		UCF-QNRF	
			MAE	RMSE	MAE	RMSE	MAE	RMSE
LSANet (Zhu et al. 2022)	0.20	14.40	66.1	110.2	8.6	13.9	112.3	186.9
<b>ZIP-P (ours)</b>	0.81	6.46	71.1	109.6	8.2	12.6	96.2	161.8
<b>ZIP-N (ours)</b>	3.36	24.73	58.8	94.6	7.7	12.1	86.4	147.6
MobileCount (Wang et al. 2020b)	3.40	16.49	89.4	146.0	9.0	15.4	131.1	222.6
LMSFFNet-XS (Yi et al. 2023)	4.58	39.28	85.8	139.9	9.2	15.1	112.8	201.6
MobleCount $\times 1.25$ (Wang et al. 2020b)	5.47	34.07	82.9	137.9	8.2	13.2	124.5	207.6
<b>ZIP-T (ours)</b>	10.53	61.39	56.3	90.5	6.6	9.9	76.0	129.4
MobleCount $\times 2$ (Wang et al. 2020b)	13.39	63.03	81.4	133.3	8.1	12.7	117.9	207.5
<b>ZIP-S (ours)</b>	33.60	242.43	55.1	88.9	5.8	9.2	73.3	125.0

Table 5: Comparison of our lightweight models with state-of-the-art lightweight approaches on ShanghaiTech A & B, and UCF-QNRF. Models are grouped by parameter size:  $< 1$  M,  $1 - 10$  M,  $10 - 20$  M,  $\geq 20$  M. FLOPs are measured on  $1920 \times 1080$  resolution. The best result in each group is highlighted, the overall best result is shown in bold.

**Ultra-lightweight ( $< 1$ M).** In this group, ZIP-P achieves the best performance across all three benchmarks, with notably lower MAE on ShanghaiTech B (8.2) and UCF-QNRF (96.2) than LSANet, despite having over 50% fewer FLOPs. This demonstrates our model’s superior design in extremely constrained settings.

**Lightweight ( $1-10$ M).** ZIP-N significantly outperforms other methods such as MobileCount and LMSFFNet-XS across all datasets. It achieves the lowest MAE in this group on ShanghaiTech A (58.8), ShanghaiTech B (7.7), and UCF-QNRF (86.4).

**Mid-size ( $10-20$ M).** ZIP-T leads this group with the best results on all benchmarks. It achieves group-best scores of 56.3 MAE on ShanghaiTech A, 6.6 on ShanghaiTech B, and 76.0 on UCF-QNRF, significantly outperforming MobileCount $\times 2$  with fewer parameters and FLOPs.

**Larger lightweight ( $\geq 20$ M).** ZIP-S sets a new benchmark in this group and across all lightweight models, achieving 55.1 MAE on ShanghaiTech A, 5.8 on ShanghaiTech B, and 73.3 on UCF-QNRF. These scores represent the best results among all compared lightweight models, and they also approach or surpass those of regular-sized models presented in Table 3.

Across all groups, our ZIP variants consistently outperform existing methods with comparable or fewer parameters and FLOPs. These results validate the effectiveness and scalability of our ZIP framework, making it suitable for real-world deployments under various computational constraints.

## Visual Comparison

We also evaluate ZIP and DMCount on the same NWPU-Crowd validation image, using an identical VGG19-based backbone for fair comparison. As shown in Fig. 6, the two density maps differ remarkably. DMCount produces elongated, ribbon-like streaks inside each dense block, which is a typical artifact of its transport-based loss. In contrast, ZIP yields compact, circular kernels that more closely resemble the point annotations, preserving the grid structure of the display. As for accuracy, DMCount under-counts the scene

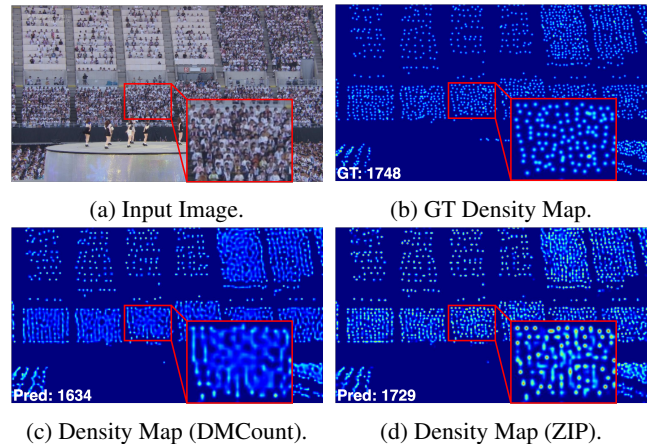


Figure 6: Qualitative comparison of DMCount and ZIP on an image from NWPU-Crowd (val). Both models utilize VGG19-based encode-decoder structure as the backbone.

by 114 heads (-6.5%), while ZIP misses only 19 heads (-1.1%), achieving a five-fold error reduction.

## Conclusion

We presented ZIP, a crowd counting framework based on zero-inflated Poisson regression. By learning a structural-zero branch to suppress background and non-head body regions, and a Poisson-rate branch to model blockwise counts, the network tackles the extreme sparsity of density maps without any explicit segmentation supervision. Comprehensive experiments show that the full model, **ZIP-B**, establishes new state-of-the-art performance on four datasets. We further introduce a family of lightweight variants (from Pico to Small) that retain these accuracy gains under tight computational budgets and consistently outperform existing models of comparable sizes on all four benchmarks, highlighting both the effectiveness and scalability of ZIP. Future work will extend ZIP to multimodal crowd counting.

## References

- Chen, I.-H.; Chen, W.-T.; Liu, Y.-W.; Yang, M.-H.; and Kuo, S.-Y. 2024. Improving point-based crowd counting and localization based on auxiliary point guidance. In *European Conference on Computer Vision*, 428–444. Springer.
- Cheng, Z.-Q.; Dai, Q.; Li, H.; Song, J.; Wu, X.; and Hauptmann, A. G. 2022. Rethinking spatial invariance of convolutional networks for object counting. In *Proceedings of the IEEE/CVF conference on computer vision and pattern recognition*, 19638–19648.
- Cherti, M.; Beaumont, R.; Wightman, R.; Wortsman, M.; Ilharco, G.; Gordon, C.; Schuhmann, C.; Schmidt, L.; and Jitsev, J. 2023. Reproducible scaling laws for contrastive language-image learning. In *Proceedings of the IEEE/CVF conference on computer vision and pattern recognition*, 2818–2829.
- Guo, M.; Yuan, L.; Yan, Z.; Chen, B.; Wang, Y.; and Ye, Q. 2024. Regressor-segmenter mutual prompt learning for crowd counting. In *Proceedings of the IEEE/CVF Conference on Computer Vision and Pattern Recognition*, 28380–28389.
- Han, T.; Bai, L.; Liu, L.; and Ouyang, W. 2023. Steerer: Resolving scale variations for counting and localization via selective inheritance learning. In *Proceedings of the IEEE/CVF International Conference on Computer Vision*, 21848–21859.
- Idrees, H.; Tayyab, M.; Athrey, K.; Zhang, D.; Al-Maadeed, S.; Rajpoot, N.; and Shah, M. 2018. Composition loss for counting, density map estimation and localization in dense crowds. In *Proceedings of the European conference on computer vision (ECCV)*, 532–546.
- Liang, D.; Xu, W.; and Bai, X. 2022. An end-to-end transformer model for crowd localization. In *European Conference on Computer Vision*, 38–54. Springer.
- Lin, H.; Ma, Z.; Hong, X.; Shangguan, Q.; and Meng, D. 2024. Gramformer: learning crowd counting via graph-modulated transformer. In *Proceedings of the AAAI Conference on Artificial Intelligence*, volume 38, 3395–3403.
- Lin, H.; Ma, Z.; Ji, R.; Wang, Y.; and Hong, X. 2022. Boosting crowd counting via multifaceted attention. In *Proceedings of the IEEE/CVF conference on computer vision and pattern recognition*, 19628–19637.
- Liu, C.; Lu, H.; Cao, Z.; and Liu, T. 2023. Point-query quadtree for crowd counting, localization, and more. In *Proceedings of the IEEE/CVF International Conference on Computer Vision*, 1676–1685.
- Liu, L.; Lu, H.; Xiong, H.; Xian, K.; Cao, Z.; and Shen, C. 2019. Counting objects by blockwise classification. *IEEE Transactions on Circuits and Systems for Video Technology*, 30(10): 3513–3527.
- Liu, W.; Salzmann, M.; and Fua, P. 2019. Context-aware crowd counting. In *Proceedings of the IEEE/CVF conference on computer vision and pattern recognition*, 5099–5108.
- Liu, Z.; Mao, H.; Wu, C.-Y.; Feichtenhofer, C.; Darrell, T.; and Xie, S. 2022. A convnet for the 2020s. In *Proceedings of the IEEE/CVF conference on computer vision and pattern recognition*, 11976–11986.
- Ma, Y.; Sanchez, V.; and Guha, T. 2024. Clip-ebc: Clip can count accurately through enhanced blockwise classification. *arXiv preprint arXiv:2403.09281*.
- Ma, Z.; Wei, X.; Hong, X.; and Gong, Y. 2019. Bayesian loss for crowd count estimation with point supervision. In *Proceedings of the IEEE/CVF international conference on computer vision*, 6142–6151.
- McCarthy, C.; Ghaderi, H.; Martí, F.; Jayaraman, P.; and Dia, H. 2025. Video-based automatic people counting for public transport: On-bus versus off-bus deployment. *Computers in Industry*, 164: 104195.
- Modolo, D.; Shuai, B.; Varior, R. R.; and Tighe, J. 2021. Understanding the impact of mistakes on background regions in crowd counting. In *Proceedings of the IEEE/CVF winter conference on applications of computer vision*, 1650–1659.
- Qin, D.; Leichner, C.; Delakis, M.; Fornoni, M.; Luo, S.; Yang, F.; Wang, W.; Banbury, C.; Ye, C.; Akin, B.; et al. 2024. MobileNetV4: universal models for the mobile ecosystem. In *European Conference on Computer Vision*, 78–96. Springer.
- Ranasinghe, Y.; Nair, N. G.; Bandara, W. G. C.; and Patel, V. M. 2024. CrowdDiff: Multi-hypothesis crowd density estimation using diffusion models. In *Proceedings of the IEEE/CVF Conference on Computer Vision and Pattern Recognition*, 12809–12819.
- Rong, L.; and Li, C. 2021. Coarse-and fine-grained attention network with background-aware loss for crowd density map estimation. In *Proceedings of the IEEE/CVF winter conference on applications of computer vision*, 3675–3684.
- Shalev-Shwartz, S.; and Ben-David, S. 2014. *Understanding machine learning: From theory to algorithms*. Cambridge university press.
- Shu, W.; Wan, J.; Tan, K. C.; Kwong, S.; and Chan, A. B. 2022. Crowd counting in the frequency domain. In *Proceedings of the IEEE/CVF conference on computer vision and pattern recognition*, 19618–19627.
- Valencia, I. J. C.; Dadios, E. P.; Fillone, A. M.; Puno, J. C. V.; Baldovino, R. G.; and Billones, R. K. C. 2021. Vision-based crowd counting and social distancing monitoring using Tiny-YOLOv4 and DeepSORT. In *2021 IEEE International Smart Cities Conference (ISC2)*, 1–7. IEEE.
- Vasu, P. K. A.; Pouransari, H.; Faghri, F.; Vemulapalli, R.; and Tuzel, O. 2024. Mobileclip: Fast image-text models through multi-modal reinforced training. In *Proceedings of the IEEE/CVF Conference on Computer Vision and Pattern Recognition*, 15963–15974.
- Wan, J.; Liu, Z.; and Chan, A. B. 2021. A generalized loss function for crowd counting and localization. In *Proceedings of the IEEE/CVF conference on computer vision and pattern recognition*, 1974–1983.
- Wang, B.; Liu, H.; Samaras, D.; and Nguyen, M. H. 2020a. Distribution matching for crowd counting. *Advances in neural information processing systems*, 33: 1595–1607.



Wang, C.; Song, Q.; Zhang, B.; Wang, Y.; Tai, Y.; Hu, X.; Wang, C.; Li, J.; Ma, J.; and Wu, Y. 2021. Uniformity in heterogeneity: Diving deep into count interval partition for crowd counting. In *Proceedings of the IEEE/CVF International Conference on Computer Vision*, 3234–3242.

Wang, P.; Gao, C.; Wang, Y.; Li, H.; and Gao, Y. 2020b. MobileCount: An efficient encoder-decoder framework for real-time crowd counting. *Neurocomputing*, 407: 292–299.

Wang, Q.; Gao, J.; Lin, W.; and Li, X. 2020c. NWPU-crowd: A large-scale benchmark for crowd counting and localization. *IEEE transactions on pattern analysis and machine intelligence*, 43(6): 2141–2149.

Wu, S.; and Yang, F. 2023. Boosting detection in crowd analysis via underutilized output features. In *Proceedings of the IEEE/CVF Conference on Computer Vision and Pattern Recognition*, 15609–15618.

Yi, J.; Shen, Z.; Chen, F.; Zhao, Y.; Xiao, S.; and Zhou, W. 2023. A lightweight multiscale feature fusion network for remote sensing object counting. *IEEE Transactions on Geoscience and Remote Sensing*, 61: 1–13.

Zhang, Y.; Zhou, D.; Chen, S.; Gao, S.; and Ma, Y. 2016. Single-image crowd counting via multi-column convolutional neural network. In *Proceedings of the IEEE conference on computer vision and pattern recognition*, 589–597.

Zhu, F.; Yan, H.; Chen, X.; and Li, T. 2022. Real-time crowd counting via lightweight scale-aware network. *Neurocomputing*, 472: 54–67.

## Supplementary Material

### Proof of Theorem 1

For a single spatial block with parameters  $\theta := (\pi, \lambda)$  constrained within a compact domain  $\Theta := [\pi_{\min}, \pi_{\max}] \times [\lambda_{\min}, \lambda_{\max}] \subset (0, 1) \times [1, \Lambda]$ , we define the **per-block negative log-likelihood** as follows<sup>1</sup>:

$$\begin{aligned}\mathcal{L}_\theta(k) &= -\log p_\theta(Y = k) \\ &= \begin{cases} -\log[\pi + (1 - \pi)e^{-\lambda}], & k = 0, \\ -\log(1 - \pi) - \lambda + k \log \lambda + \log k!, & k \geq 1. \end{cases}\end{aligned}$$

Given this formulation, we establish the following regularity property of  $\mathcal{L}_\theta(k)$ .

**Lemma 1.** *The per-block negative log-likelihood  $\mathcal{L}_\theta(k)$  is  $l$ -Lipschitz continuous with respect to the discrete count variable  $k$ , for all  $k \in \{0, 1, \dots, k_{\max}\}$  and  $\theta \in \Theta$ , where  $\Theta \subset (0, 1) \times [1, \Lambda]$  is a compact parameter space<sup>2</sup>.*

*Proof.* **Case 1:** For  $k = 0$ , we compute:

$$\begin{aligned}|\mathcal{L}_\theta(1) - \mathcal{L}_\theta(0)| &= \left| \log \left( \frac{\pi + (1 - \pi)e^{-\lambda}}{1 - \pi} \right) + \lambda - \log \lambda \right| \\ &\leq \left| \log \left( \frac{\pi + (1 - \pi)e^{-\lambda}}{1 - \pi} \right) \right| + |\lambda - \log \lambda| \quad (14)\end{aligned}$$

$$= l_1(\pi, \lambda) + l_2(\lambda), \quad (15)$$

where

$$l_1(\pi, \lambda) := \left| \log \left( \frac{\pi + (1 - \pi)e^{-\lambda}}{1 - \pi} \right) \right|$$

and

$$l_2(\lambda) := |\lambda - \log \lambda|.$$

To bound  $l_1(\pi, \lambda)$ , observe that

$$0 < e^{-\lambda_{\max}} \leq \pi + (1 - \pi)e^{-\lambda} \leq 1$$

and

$$0 < 1 - \pi_{\max} \leq 1 - \pi \leq 1 - \pi_{\min}.$$

Thus, we have

$$0 < \frac{e^{-\lambda_{\max}}}{1 - \pi_{\min}} \leq \frac{\pi + (1 - \pi)e^{-\lambda}}{1 - \pi} < \frac{1}{1 - \pi_{\max}},$$

<sup>1</sup>Since  $\pi$  is computed by applying a sigmoid activation to the output of a neural head, it naturally lies in the open interval  $(0, 1)$ . In practice, we can further restrict  $\pi$  to a closed subinterval  $[\pi_{\min}, \pi_{\max}] \subset (0, 1)$  by employing techniques such as output clipping, batch normalization, or weight regularization to ensure the logits remain within bounded ranges. For the Poisson rate parameter  $\lambda$ , it is defined as a weighted average over a finite set of positive and finite bin centers  $\{b_k\}_{k=2}^n$  (refer to Eq. (4)). Consequently, we can ensure that  $\lambda \in [\lambda_{\min}, \lambda_{\max}]$ , where  $1 \leq b_2 \leq \lambda_{\min} \leq \lambda_{\max} \leq b_n < \infty$ .

<sup>2</sup>In practice,  $k_{\max}$  is upper-bounded by the number of pixels in each block, since it is physically implausible for more than one person to occupy a single pixel.

which implies

$$l_1(\pi, \lambda) \leq \max \left( \left| \log \left( \frac{e^{-\lambda_{\max}}}{1 - \pi_{\min}} \right) \right|, \left| \log \left( \frac{1}{1 - \pi_{\max}} \right) \right| \right)$$

For  $l_2(\lambda)$ , note that  $\lambda - \log \lambda$  is monotonically increasing for  $\lambda \geq 1$ , so

$$1 \leq \lambda_{\min} - \log \lambda_{\min} \leq \lambda - \log \lambda \leq \lambda_{\max} - \log \lambda_{\max},$$

and therefore

$$l_2(\lambda) \leq \lambda_{\max} - \log \lambda_{\max}.$$

Combining these bounds yields:

$$|\mathcal{L}_\theta(1) - \mathcal{L}_\theta(0)| \leq u_1 + u_2, \quad (16)$$

where

$$u_1 := \max \left( \left| \log \left( \frac{e^{-\lambda_{\max}}}{1 - \pi_{\min}} \right) \right|, \left| \log \left( \frac{1}{1 - \pi_{\max}} \right) \right| \right)$$

and

$$u_2 := \lambda_{\max} - \log \lambda_{\max}.$$

**Case 2:** For  $k \in [1, \lambda_{\max} - 1]$ , we have:

$$|\mathcal{L}_\theta(k+1) - \mathcal{L}_\theta(k)| = \left| \log \frac{k+1}{\lambda} \right| \leq \log \left( \frac{k_{\max} + 1}{\lambda_{\min}} \right),$$

where  $k_{\max}$  denotes the largest observed count in any block within the training set.

Let  $u_3 := \log((k_{\max} + 1)/\lambda_{\min})$ , and define the Lipschitz constant  $l$  as:

$$l := \max(u_1 + u_2, u_3).$$

Then, for all  $k \in [0, \lambda_{\max} - 1]$ , the per-block negative log-likelihood satisfies:

$$|\mathcal{L}_\theta(k+1) - \mathcal{L}_\theta(k)| \leq l,$$

implying that the per-block NLL  $\mathcal{L}_\theta$  is  $l$ -Lipschitz continuous.  $\square$

Following Wang et al., we flatten the spatial dimensions to avoid cluttered notations. Let  $s := hw$  denote the total number of spatial blocks in a single image. Define the **full-image negative log-likelihood** as:

$$\mathcal{L}_{\text{NLL}}(\mathbf{z}; \boldsymbol{\theta}) = \frac{1}{s} \sum_{i=1}^s \mathcal{L}_{\theta_i}(\mathbf{z}_i), \quad (17)$$

where  $\mathbf{z} = (\mathbf{z}_1, \dots, \mathbf{z}_s)$  is the vector of discrete blockwise counts, and  $\boldsymbol{\theta} = (\boldsymbol{\theta}_1, \dots, \boldsymbol{\theta}_s)$  are the corresponding model parameters per block, with each  $\boldsymbol{\theta}_i = (\pi_i, \lambda_i) \in \Theta$ . Note that Eq. (17) is the flattened version of Eq. (7). We now state the following results.

**Lemma 2.** *The full-image negative log-likelihood  $\mathcal{L}_{\text{NLL}}(\mathbf{z}; \boldsymbol{\theta})$  is  $L$ -Lipschitz continuous with respect to the joint  $\mathcal{L}_1$  norm over  $(\mathbf{z}, \boldsymbol{\theta})$ .*

*Proof.* Let  $(z, \theta)$  and  $(z', \theta)'$  be two annotation-parameter pairs. Then

$$\begin{aligned} & \left| \mathcal{L}_{\text{NLL}}(z; \theta) - \mathcal{L}_{\text{NLL}}(z'; \theta') \right| \\ &= \left| \frac{1}{s} \sum_{i=1}^s (\mathcal{L}_{\theta_i}(z_i) - \mathcal{L}_{\theta'_i}(z'_i)) \right| \\ &\leq \frac{1}{s} \sum_{i=1}^s |\mathcal{L}_{\theta_i}(z_i) - \mathcal{L}_{\theta_i}(z'_i)| + \frac{1}{s} \sum_{i=1}^s |\mathcal{L}_{\theta_i}(z'_i) - \mathcal{L}_{\theta'_i}(z'_i)| \end{aligned}$$

By Lemma 1, the per-block loss  $\mathcal{L}_{\theta}(k)$  is  $l$ -Lipschitz in  $k$ , so the first term is bounded by:

$$\frac{1}{s} \sum_{i=1}^s l \|z_i - z'_i\|_1 = l \cdot \frac{1}{s} \|z - z'\|_1.$$

For the second term, since  $\Theta$  is compact and  $\mathcal{L}_{\theta}(k)$  is differentiable in  $\theta$ , we define

$$M := \sup_{k, \theta} \|\nabla_{\theta} \mathcal{L}_{\theta}(k)\| < \infty,$$

which yields

$$|\mathcal{L}_{\theta_i}(z'_i) - \mathcal{L}_{\theta'_i}(z'_i)| \leq M \cdot \|\theta_i - \theta'_i\|_1.$$

Summing over all  $i$ , we obtain

$$\frac{1}{s} \sum_{i=1}^s |\mathcal{L}_{\theta_i}(z'_i) - \mathcal{L}_{\theta'_i}(z'_i)| \leq M \cdot \frac{1}{s} \|\theta - \theta'\|_1.$$

Combining both terms gives:

$$|\mathcal{L}_{\text{NLL}}(z; \theta) - \mathcal{L}_{\text{NLL}}(z'; \theta')| \leq \frac{l}{s} \|z - z'\|_1 + \frac{M}{s} \|\theta - \theta'\|_1$$

Thus,

$$|g(z; \theta) - g(z'; \theta')| \leq L \| (z, \theta) - (z', \theta') \|_1,$$

where  $L := (l + M)/s < \infty$ .  $\square$

As in the supplement of (Wang et al. 2020a), we treat the crowd counting model as consisting of  $s$  independent scalar regressors, one for each spatial block in the image. Let  $\mathcal{S} := \{(\mathbf{X}^{(k)}, z^{(k)})\}_{k=1}^K$  denote a random draw of  $K$  training examples from the training set  $\mathcal{D}$ . Let  $\mathcal{F}'$  denote the hypothesis class that mapping an image  $\mathbf{X}$  to a vector of block-wise distribution parameters  $\theta$ . Let  $\mathcal{L}_{\text{NLL}}$  be the ZIP loss aggregation function defined in Eq. (17). By Lemma E(b) in (Wang et al. 2020a), if each  $\mathcal{L}_{\text{NLL}}$  is  $L$ -Lipschitz continuous with respect to its input, then the empirical Rademacher complexity of the composed class is bounded as

$$\mathcal{R}_{\mathcal{S}}(\mathcal{L}_{\text{NLL}} \circ \mathcal{F}') \leq L \cdot s \cdot \mathcal{R}_{\mathcal{S}}(\mathcal{H}),$$

where  $\mathcal{H}$  is the shared hypothesis class for the base feature extractor and prediction head across all blocks, and  $\mathcal{R}_{\mathcal{S}}$  denotes the empirical Rademacher complexity with respect to sample  $\mathcal{S}$ . Now, applying Theorem 26.5 from (Shalev-Shwartz and Ben-David 2014) to the composed function  $\mathcal{L}_{\text{NLL}} \circ f_{\mathcal{S}}^{\text{ZIP}}$ , we obtain the following generalization bound.

Suffix	MAE	M1Pro CPU	M1Pro GPU	5900X	3090
-P	8.23	9.99	118.63	122.22	1,012.01
-N	7.74	5.28	63.17	50.67	548.14
-T	6.67	1.87	27.77	18.37	249.73
-S	5.83	0.48	6.80	4.60	50.91

Table 6: Inference speed (frames per second, FPS) of the lightweight variants on ShanghaiTech B ( $1024 \times 768$  resolution). Results are reported on four hardware platforms.

For any  $\delta \in (0, 1)$ , with probability at least  $1 - \delta$  over  $\mathcal{S}$ , the expected risk is bounded by:

$$\begin{aligned} \mathcal{R}_{\mathcal{D}}(f_{\mathcal{S}}^{\text{NLL}}, \mathcal{L}_{\text{NLL}}) &\leq \mathcal{R}_{\mathcal{D}}(f_{\mathcal{D}}^{\text{NLL}}, \mathcal{L}_{\text{NLL}}) + 2 \cdot L \cdot s \cdot \mathcal{R}_{\mathcal{S}}(\mathcal{H}) + \\ &\quad 5B_{\text{NLL}} \sqrt{\frac{2 \log(8/\delta)}{K}}, \end{aligned}$$

where

- $f_{\mathcal{S}}^{\text{NLL}}$  is the model learned from training sample  $\mathcal{S}$ ,
- $f_{\mathcal{D}}^{\text{NLL}}$  is the population risk minimizer under the loss  $\mathcal{L}_{\text{NLL}}$ ,
- $L$  is the Lipschitz constant of the loss function  $\mathcal{L}_{\text{NLL}}$ ,
- $s$  is the number of blocks per image,
- $B_{\text{NLL}} = \sup_{\mathbf{X}, z} \mathcal{L}_{\text{NLL}}(z, f(\mathbf{X})) < \infty$  is the uniform upper bound on the ZIP NLL loss, guaranteed due to the compactness of  $\Theta$  and the bounded support of the count vector  $z$ .

**Remark.** Since the cross-entropy loss in Eq. (5) is 1-Lipschitz under the  $\mathcal{L}_1$  norm, its empirical Rademacher complexity is bounded by  $s_+ \cdot \mathcal{R}_{\mathcal{S}}(\mathcal{H})$ , where  $s_+$  denotes the number of blocks with nonzero counts (i.e.,  $z_i > 0$ ) and  $0 \leq s_+ \leq s$ .

Combining this with the generalization bound for the counting loss in Wang et al. (2020a), we obtain the following generalization error bound for the total loss in Eq. (11):

$$\begin{aligned} \mathcal{R}_{\mathcal{D}}(f_{\mathcal{S}}^{\text{total}}, \mathcal{L}_{\text{total}}) &\leq \mathcal{R}_{\mathcal{D}}(f_{\mathcal{D}}^{\text{total}}, \mathcal{L}_{\text{total}}) + \\ &\quad 2 \cdot (L \cdot s + s + \omega s_+) \cdot \mathcal{R}_{\mathcal{S}}(\mathcal{H}) + \\ &\quad 5B \sqrt{\frac{2 \log(8/\delta)}{K}}, \end{aligned}$$

where  $B = B_{\text{NLL}} + B_{\text{CE}} + B_{\text{count}}$  denotes the sum of the uniform upper bounds of Eq. (7), Eq. (5) and Eq. (10).

## Inference Speed

To assess the practical deployment potential of our lightweight models, we measure the average inference speed of each ZIP variant across four representative hardware platforms: Apple M1 Pro CPU (6 performance + 2 efficiency cores), Apple M1 Pro 14-core GPU, AMD Ryzen 9 5900X CPU (12-core), and NVIDIA RTX 3090 GPU. All experiments are conducted on the ShanghaiTech B dataset using full-precision inference at an input resolution of  $1024 \times 768$ , which reflects real-world surveillance camera scenarios. Inference speed is computed as the reciprocal of the average per-image inference time, where the time is measured individually for each test image. The PyTorch version is 2.7.1.



Dataset	Training Size	Block Size	Scale Range	Brightness	Contrast	Saturation	Saltiness	Spiciness
ShanghaiTech A	224	16	[0.75, 2.0]	0.15	0.15	0.10	0.001	0.001
ShanghaiTech B	448	16	[0.75, 2.5]	0.15	0.15	0.10	0.001	0.001
UCF-QNRF	672	32	[0.75, 2.0]	0.15	0.15	0.10	0.001	0.001
NWPU-Crowd	672	16	[0.75, 2.0]	0.20	0.20	0.15	0.001	0.001

Table 7: Dataset-specific data augmentation settings used during training. Each dataset is augmented using a tailored configuration of training resolution, block granularity, and perturbation strengths. The cropping scale controls spatial zoom variation, while brightness, contrast, and saturation simulate photometric noise. Saltiness and spiciness introduce localized binary corruption to enhance robustness.

Table 6 reports the average frames per second (FPS) for each model. Our smallest variant, ZIP-P, achieves the highest throughput on all platforms, reaching 122.22 FPS on AMD 5900X and over 1,000 FPS on RTX 3090, making it ideal for resource-constrained or real-time applications. On the other end, ZIP-S delivers the best accuracy (MAE = 5.83) but at a higher computational cost, with CPU-side inference limited to under 5 FPS, making it suitable for accuracy-critical but latency-tolerant use cases. ZIP-N and ZIP-T offer compelling accuracy-efficiency trade-offs. For example, ZIP-T achieves 18.37 FPS on AMD 5900X and 249.73 FPS on RTX 3090, while maintaining a competitive MAE of 6.67. These results indicate that mid-sized variants can enable near real-time performance even on high-end CPUs without requiring dedicated GPUs. Overall, our ZIP family provides a scalable solution space, allowing deployment under varying hardware and latency constraints without compromising on count accuracy.

## Datasets and Augmentation

**Datasets.** ShanghaiTech A & B (Zhang et al. 2016), UCF-QNRF (Idrees et al. 2018), and NWPU-Crowd (Wang et al. 2020c) are four widely used crowd counting benchmarks. ShanghaiTech A contains 300 training images and 182 test images, with highly congested scenes and an average of 501 people per image. ShanghaiTech B, the only dataset collected from surveillance viewpoints, includes 400 training and 316 test images, featuring relatively sparse crowds. UCF-QNRF comprises 1,201 training images and 334 test images with extremely dense crowds, averaging 815 people per image. NWPU-Crowd is currently the largest high-resolution crowd counting dataset, containing 3,109 training images, 500 validation images, and 1,500 test images, with an average count of 418. The test set annotations of NWPU-Crowd are not publicly released. To obtain evaluation results on this split, predicted counts must be submitted to the official evaluation server. This protocol helps maintain a fair comparison between methods by preventing result tweaking using test labels.

We apply a combination of data augmentation techniques during training, largely following the EBC framework (Ma, Sanchez, and Guha 2024). The transformation pipeline includes the following operations:

- **RandomResizedCrop:** For each image, we randomly select a cropping scale  $s$  from a predefined range  $[s_{\min}, s_{\max}]$ . A region of size `train_size`  $\times$   $s$  is

cropped and then resized back to `train_size`. This operation effectively amplifies the large blockwise count values, which follow a long-tailed distribution.

- **RandomHorizontalFlip:** The image is flipped horizontally with a probability of 0.5.
- **ColorJitter:** Brightness, contrast, and saturation are independently perturbed within specified ranges to simulate varying lighting and color conditions. Hue adjustment is disabled (set to 0.0). We use the implementation from `torchvision` to achieve this augmentation.
- **PepperSaltNoise:** A small fraction of pixels are randomly replaced with either black (salt, value 0) or white (pepper, value 1), introducing local binary noise. The noise levels are controlled by two parameters: saltiness (ratio of salt pixels) and spiciness (ratio of pepper pixels). These two parameters are fixed to 0.001 across all datasets.

We use different values for training resolution, block sizes and augmentation ranges, and the details are presented in Table 7.

## Bin Configurations

To accommodate varying count distributions across datasets, the blockwise ground-truth counts were quantized into dataset-specific integer bins. Each bin is defined as a closed interval  $[a, b]$  corresponding to a discrete count range, and its associated bin center is used to estimate the expected value within the ZIP framework. The following configurations were adopted for each dataset:

- **ShanghaiTech A (block size = 16):** The counts were discretized into 14 bins: 11 singleton bins for counts from 0 to 10, two intermediate bins  $[11, 12]$  and  $[13, 14]$ , and one final bin  $[15, \infty)$  to cover the long tail of larger counts. The corresponding bin centers were: 0.0, 1.0, 2.0, 3.0, 4.0, 5.0, 6.0, 7.0, 8.0, 9.0, 10.0, 11.38, 13.38, and 16.26, where the final three values were computed as the empirical means within each multi-count interval.
- **ShanghaiTech B (block size = 16):** A more compact binning scheme was used, reflecting the relatively sparse nature of the dataset. Ten bins were defined: eight singleton bins for counts 0 through 8 and one open-ended bin  $[9, \infty)$ . The bin centers were: 0.0, 1.0, 2.0, 3.0, 4.0, 5.0, 6.0, 7.0, 8.0, 10.16.
- **UCF-QNRF (block size = 32):** To model the highly dense and skewed count distribution, a fine-grained bin-

Method	Luminance-Level			Scene-Level			
	L1	L2	L3	S1	S2	S3	S4
CrowdHat (Wu and Yang 2023)	19.13	19.63	13.04	19.36	18.62	14.64	21.69
STEERER (Han et al. 2023)	<b>14.37</b>	14.26	9.90	16.67	11.28	12.22	23.66
APGCC (Chen et al. 2024)	31.57	22.07	17.28	36.10	14.72	14.13	29.33
CLIP-EBC (Ma, Sanchez, and Guha 2024)	16.47	15.55	11.88	20.69	11.81	<u>12.10</u>	22.13
<b>ZIP-B (ours)</b>	<u>14.49</u>	<b>11.23</b>	<b>8.26</b>	<b>11.13</b>	<b>9.97</b>	<b>11.61</b>	<b>21.57</b>

Table 8: NAE (%) comparison of ZIP-B with the latest methods on the NWPU-Crowd test set under different luminance levels and scene densities. The best result within each subgroup is shown in **bold**, and the second best is underlined. ZIP-B achieves the lowest NAE across most subgroups, demonstrating robustness to lighting and crowd scale variations.

ning strategy was adopted. The counts were divided into 21 bins: 11 singleton bins (0–10), followed by progressively wider intervals up to  $[34, \infty)$ . The corresponding bin centers included both integers and empirically estimated means for the aggregated bins: 0.0, 1.0,  $\dots$ , 10.0, 11.43, 13.43, 15.44, 17.44, 19.43, 21.83, 24.85, 27.87, 31.24, 38.86.

- **NWPU-Crowd (block size = 16):** A simplified 11-bin scheme was employed, with singleton bins from 0 to 9 and one catch-all bin  $[10, \infty)$  to handle outliers. The bin centers were: 0.0, 1.0,  $\dots$ , 9.0, 12.16, where the last center reflects the average count in the aggregated tail.

### Luminance-Level and Scene-Level Comparison

To further evaluate the robustness and generalizability of ZIP-B, we conduct a detailed analysis on the NWPU-Crowd test set, stratifying the results by both luminance levels and scene density levels. Luminance was measured using the average pixel intensity in the Y channel of the YUV color space, and divided into three groups: L1  $[0, 0.25]$ , L2  $(0.25, 0.5]$ , and L3  $(0.5, 0.75]$ . Scene-level difficulty was assessed based on the ground-truth number of people per image, grouped into four intervals: S1  $(0, 100]$ , S2  $(100, 500]$ , S3  $(500, 5000]$  and S4  $(> 5000)$ . Performance was measured using Normalized Absolute Error (NAE), reported in percentage.

As shown in Table 8, ZIP-B consistently outperforms prior methods across six out of seven subgroups, achieving the lowest NAE in L2 (11.23%), L3 (8.26%), and all four scene levels (S1–S4), showing that ZIP-B is not only accurate on average, but also **robust across varying lighting conditions and crowd densities**. In particular, it shows notable gains under sparse scenes (S1), demonstrating the effectiveness of the zero-inflated Poisson modeling.

### Effect of Training Resolution and Block Size on UCF-QNRF

We study the impact of varying the training input resolution and block size on model performance using the UCF-QNRF dataset and the VGG19-based encoder-decoder structure. The results are presented in Table 9.

Across all training resolutions, using a larger block size of 32 consistently yields better performance than a block size of 16 in terms of both MAE and RMSE. For instance,

Training Size	Block Size			
	16		32	
	MAE	RMSE	MAE	RMSE
<b>448</b>	78.52	130.24	75.73	127.17
<b>672</b>	75.06	131.62	<b>73.02</b>	<b>126.11</b>
<b>896</b>	77.92	133.65	75.69	130.30

Table 9: Impact of training resolution and block size on UCF-QNRF with the VGG19-based backbone. Using a larger block size (32) consistently improves MAE and RMSE across resolutions. The best overall performance is achieved with a resolution of 672 and block size 32, highlighting the benefit of coarser spatial supervision for high-resolution dense crowd scenes.

at a resolution of 672, the configuration with block size 32 achieves the best overall performance, with an MAE of 73.02 and a RMSE of 126.11. This suggests that for UCF-QNRF—a dataset with high-resolution images and dense crowd scenes—larger blocks better capture spatially aggregated count patterns, possibly providing more stable supervision.

While increasing the training resolution generally improves RMSE slightly, the gains saturate or diminish beyond 672. This might be attributed to the sampling behavior of RandomResizedCrop and how it interacts with image and block sizes. At lower resolutions (e.g., 448), cropped regions often lack sufficient spatial coverage to include high-density areas, resulting in a limited number of blocks with large counts. This weakens supervision on the tail of the count distribution. On the other hand, at very high resolutions (e.g., 896), the upper end of the cropping scale becomes ineffective, as attempting to crop regions larger than the image leads to upscaling followed by near-trivial cropping and resizing. This process fails to increase the sample sizes of large blockwise counts and may introduce resampling artifacts, which together limit the benefits of increased resolution. These observations explain why intermediate resolutions (e.g., 672) paired with a coarser block size (e.g., 32) achieve the best overall results on UCF-QNRF.

Method	ShanghaiTech A		ShanghaiTech B		UCF-QNRF		NWPU-Crowd (Val)	
	MAE	RMSE	MAE	RMSE	MAE	RMSE	MAE	RMSE
BL (Ma et al. 2019)	62.8	101.8	7.7	12.7	88.7	154.8	93.6	470.3
DMCount (Wang et al. 2020a)	<u>59.7</u>	95.7	7.4	11.8	85.6	148.3	70.5	357.6
GL (Wan, Liu, and Chan 2021)	61.3	<u>95.4</u>	7.3	11.7	84.3	147.5	-	-
EBC (Ma, Sanchez, and Guha 2024)	62.3	<u>98.9</u>	<u>7.0</u>	<u>10.9</u>	<u>77.2</u>	<u>130.4</u>	<u>39.6</u>	<u>95.8</u>
<b>ZIP (ours)</b>	<b>58.7</b>	<b>93.6</b>	<b>6.0</b>	<b>9.9</b>	<b>73.0</b>	<b>126.1</b>	<b>38.3</b>	<b>90.3</b>
Improvement over EBC	5.9%	2.9%	14.2%	9.1%	5.4%	3.2%	3.2%	5.7%

Table 10: Overall comparison of ZIP with other frameworks on ShanghaiTech A & B, UCF-QNRF and NWPU-Crowd. All frameworks use the VGG19-based backbone. Results demonstrate that our framework ZIP significantly outperforms other methods, achieving the lowest MAE and RMSE on all four benchmarks. Our ZIP also consistently improves the EBC framework, at most by 14.2%. The best results are highlighted in **bold** font, and the second best results are underscored.

Suffix	Size (M)	ShanghaiTech A			ShanghaiTech B			UCF-QNRF		
		MAE	RMSE	NAE (%)	MAE	RMSE	NAE (%)	MAE	RMSE	NAE (%)
-P	0.81	71.18	109.60	16.69	8.23	12.62	6.98	96.29	161.82	14.40
-N	3.36	58.86	94.63	14.15	7.74	12.14	6.33	86.46	147.64	12.60
-T	10.53	56.36	90.55	13.26	6.67	9.90	5.52	76.02	129.40	11.10
-S	33.60	<u>55.17</u>	<u>88.99</u>	<u>11.97</u>	<u>5.83</u>	<u>9.21</u>	<u>4.58</u>	<u>73.32</u>	<u>125.09</u>	<u>10.40</u>
-B	105.60	<b>47.81</b>	<b>75.04</b>	<b>11.06</b>	<b>5.51</b>	<b>8.63</b>	<b>4.48</b>	<b>69.46</b>	<b>121.88</b>	<b>10.18</b>

Table 11: Comparison of all ZIP variants on ShanghaiTech A & B, and UCF-QNRF. Best results are shown in the **bold** typeface and the second best are underlined.

## Robustness to Random Seed Initialization

To assess the robustness of the proposed ZIP-B model with respect to random initialization, an additional experiment was conducted by training ZIP-B on the NWPU-Crowd validation split using five different random seeds: 1, 42, 1234, 3407, and 12345. This dataset was selected due to its large size (500 instances), which offers a more statistically stable evaluation compared to other benchmarks. The model achieved a mean MAE of 29.00 with a standard deviation of 0.83, indicating low sensitivity to random initialization. For comparison, the result reported in Table 3 for ZIP-B on NWPU-Crowd (val) is a single-run MAE of 28.2. The fact that this value falls within one standard deviation of the mean observed across five seeds confirms that the previously reported performance is representative and not an outlier due to a favorable random initialization. These results underscore the stability and reliability of the ZIP framework under common sources of stochasticity during training.

## Overall Comparison of Frameworks

We compare ZIP with several existing frameworks on the four benchmarks, shown in Table 10. All methods are based on the same VGG19 backbone. Our approach sets a new state-of-the-art on ShanghaiTech A & B, UCF-QNRF and NWPU-Crowd. Notably, when compared directly with its EBC baseline, our ZIP model demonstrates significant performance gains across all datasets, reducing the MAE by a margin of 3.2% to 14.2%. These improvements validate the efficacy of zero-inflated Poisson regression for counting.

## Comparison of All ZIP Variants

Table 11 reports the full results of the five ZIP variants: Pico (-P), Nano (-N), Tiny (-T), Small (-S) and Base (-B), on ShanghaiTech A, ShanghaiTech B and UCF-QNRF. The variants differ only in backbone capacity (from 0.8 M to 105 M parameters); all heads, losses and training settings are identical. From this table, we can observe three trends:

- **Monotonic accuracy gain with scale.** From -P to -B every step produces lower error on all datasets. MAE on ShanghaiTech A drops from 71.2 to 47.8 (-32.8%), while UCF-QNRF MAE falls from 96.3 to 69.5 (-27.8%). A similar monotone decrease is observed for RMSE and NAE.
- **Diminishing returns.** The relative improvement per additional million parameters shrinks after the -T model (10 M). For example, moving from -T to -S cuts ShanghaiTech A MAE by 3.7% whereas the jump from -N to -T yields  $1.7\times$  that reduction with fewer added parameters. This suggests that -T or -S may offer the best accuracy-efficiency trade-off for many deployments.
- **Consistent generalization across datasets.** Ranking of variants is identical on ShanghaiTech A/B and UCF-QNRF, indicating that gains are not dataset-specific but stem from the scalable ZIP formulation itself.

Overall, the results demonstrate that ZIP scales gracefully: the smallest model remains competitive for edge devices, whereas the largest model achieves state-of-the-art accuracy.





Figure 7: Examples of annotation noise in NWPU-Crowd. Left column: input images with zoom-in views of the regions outlined in red. Center column: ground-truth density map with total count. Right column: density map with total count predicted by ZIP-B. Top row: mirror reflections labeled as real people. Middle row: photo-realistic audience on a display screen left unlabeled. Bottom row: snow-covered tree branches mislabeled as a dense crowd.

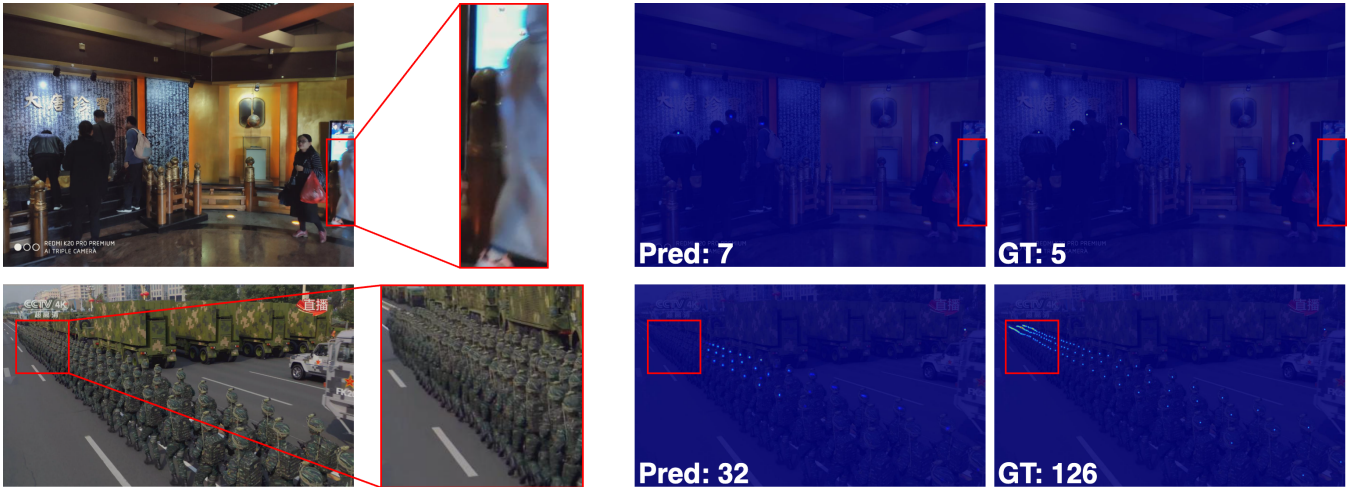


Figure 8: Two typical failure cases of ZIP-B. Left: input image with a zoom-in of the critical region (red box). Center: predicted density map with total count. Right: ground-truth density map with total count.

## Annotation Noise

Although NWPU-Crowd is currently the largest high-resolution benchmark, we observed non-negligible label noise. Fig. 7 presents three typical failure modes on the validation split of this dataset: over-labeled reflections (top row), under-labeled screen display (middle row), and complex natural textures being mislabeled as crowds (bottom row).

In the top row, the red box highlights strong reflections of pedestrians on a glass facade. These mirror images have

been annotated as real heads, yet they are visually less consistent with surrounding people, resulting a total count of 439. ZIP-B correctly ignores the reflections, producing a lower but more realistic count of 272.

The middle row depicts a conference hall is shown on a large display. The audience visible inside the screen looks photo-realistic, but none of these heads are annotated (GT = 221). The model nevertheless detects them, yielding a higher prediction (671). Qualitatively, the additional detections cor-

respond to the people shown on the screen.

In the bottom row, a snowy park scene is shown where the red box highlights complex textures on snow-covered tree branches. These natural textures have been mistakenly annotated as a dense crowd in the background, leading to a grossly overestimated ground truth count of 993. Our model is more robust to this type of noise, largely ignoring the mis-labeled texture and predicting a more plausible count of 448.

These examples underline two points: (i) reported errors can stem from annotation artifacts rather than model failure, and (ii) the structural-zero + ZIP formulation is robust enough to down-weight unrealistic cues while still detecting plausible but unlabeled heads. Future benchmarks would benefit from more consistent annotation protocols, confidence tags to flag uncertain regions, and a multi-annotator verification process to improve label quality and consistency.

### Failure Analysis

Despite its overall strong performance, ZIP-B still fails under certain visual ambiguities. Fig. 8 highlights two typical errors. The top row corresponds to false positive on man-shaped artifact: in an indoor museum scene, a post along the rope barrier closely resembles a standing person in both shape and color, and as a result, ZIP-B misclassifies the post as a human. In the bottom row, rows of soldiers wear camouflage that blends with the background trucks. Although nearby soldiers are detected reliably, the model fails to pick up many small, low-contrast heads in the far field, leading to an under-count of -94. These failure cases suggest that incorporating additional sensing modalities, particularly infrared imagery, may help suppress person-like artifacts and recover low-contrast targets, thereby reducing both false positives and false negatives. Exploring how the ZIP formulation can be extended to multi-modal crowd counting will be an important direction for our future work.

### Blockwise Count Distribution

For each dataset’s **training split**, we form a pixel-level density map by placing 1 at each annotated head location and 0 elsewhere, without Gaussian smoothing being applied. We then slide an axis-aligned  $B \times B$  window over the map with stride 1 pixel and record the integer count equal to the sum of densities in that window (equivalently, the number of annotated heads whose pixel coordinates fall inside the window). We repeat for  $B \in \{8, 16, 32\}$  and aggregate counts over all windows from all images, converting to percentages. Fig. 9 illustrates the results. As the block size (window size)  $B$  increases, zero percentages drop because each window integrates over a larger receptive field and is therefore more likely to include at least one head annotation. However, even at  $B=32$  the distributions remain heavily zero-inflated. For instance,  $> 80\%$  zeros in UCF-QNRF and  $> 90\%$  in ShanghaiTech B and NWPU-Crowd. This indicates that annotation sparsity is a persistent regime rather than an artifact of using very fine windows. Note that increasing  $B$  also coarsens supervision: spatial detail about where heads occur *within* a window is lost, making it harder for a crowd counting model to localize density peaks and learn fine-grained cues. In the

extreme limit,  $B$  equal to the entire image collapses supervision to a single global count label; the learning problem degenerates to (image-level) weakly supervised counting with no spatial guidance at all. Our ZIP formulation is motivated by operating in the practically useful regime of relatively small block size, where supervision is highly sparse yet still spatially informative, necessitating an explicit treatment of excess zeros.

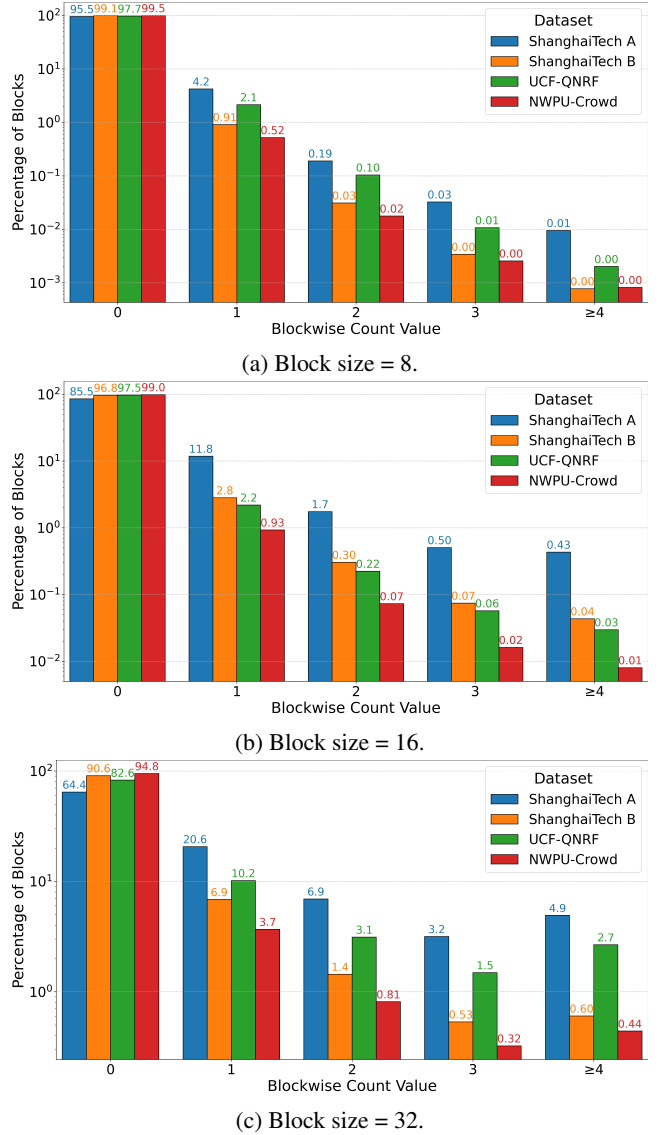


Figure 9: Blockwise count distributions across common crowd counting benchmarks at different block sizes (8, 16, 32). For each dataset, we first generate ground-truth pixel-level density maps from point annotations, without using Gaussian smoothing. Then, we slide a  $B \times B$  window with stride 1 across the map, summing the density within the window to obtain its count. Bars show the percentage of windows with count values 0, 1, 2, 3,  $\geq 4$  (log-scale  $y$ -axis).



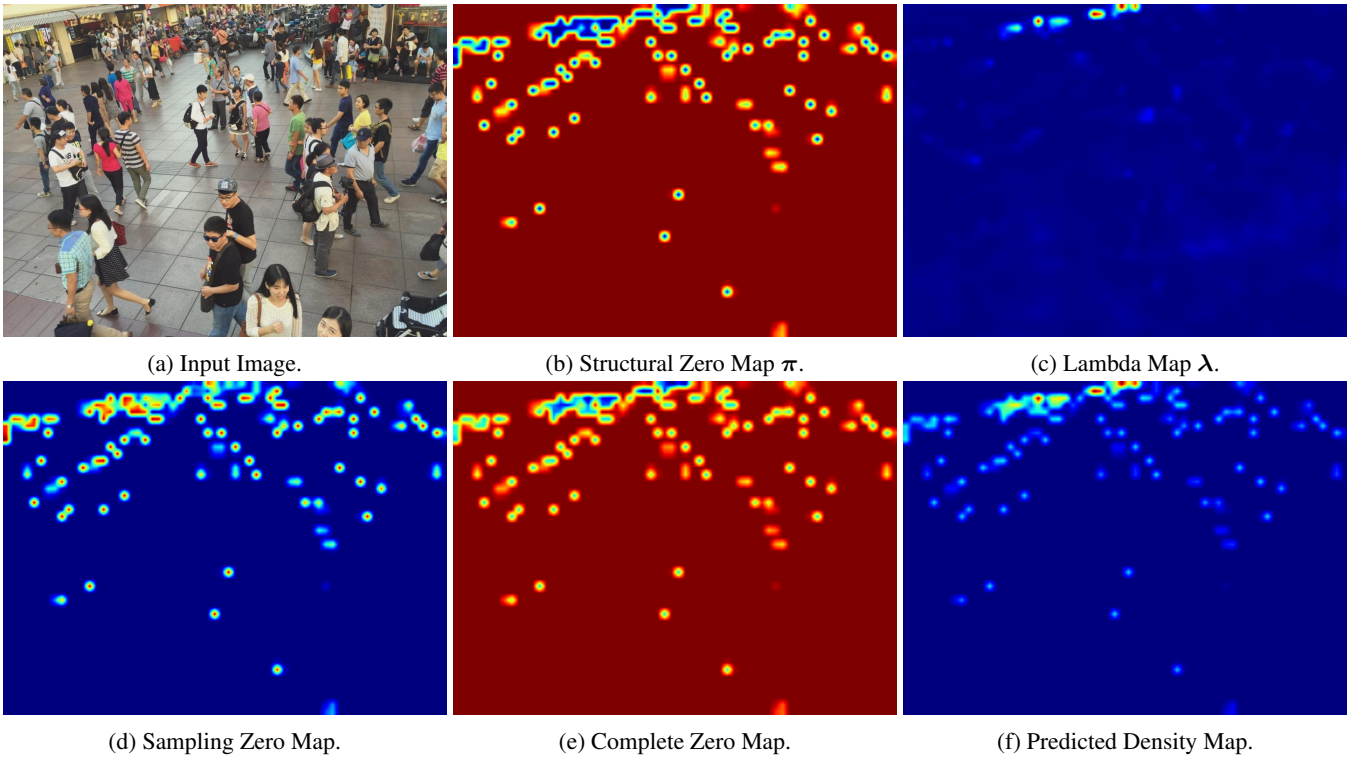


Figure 10: Visualization of the interpretability of our ZIP framework. This figure decomposes ZIP-B’s prediction on a test image from ShanghaiTech B into its key components, illustrating how the model separates structurally irrelevant regions from informative ones. (a) Input Image: A representative test image from the ShanghaiTech B dataset. (b) Structural Zero Map  $\pi$ : Shows the model’s estimated probability that a block is structurally empty (e.g., background, non-head regions). Red regions indicate high structural-zero probability, while blue/cyan spots highlight likely head-center regions, effectively masking irrelevant areas like pavement. (c) Lambda Map  $\lambda$ : The predicted Poisson rate map, representing expected counts per block. (d) Sampling Zero Map: Visualizes the probability of zero counts due to sampling error (*i.e.*, head-center blocks receive zero counts due to the point-based labels). Computed as  $(1 - \pi) \otimes \exp(-\lambda)$ , it peaks at sparser head-center regions. (e) Complete Zero Map: The total probability of a zero count from any source, combining both structural and sampling zeros. (f) Predicted Density Map  $Y^*$ : The final predicted density map, computed as  $(1 - \pi) \otimes \lambda$ , integrating both spatial suppression and expected counts. Together, these visualizations show how ZIP disentangles *where* people are located from *how densely* they are present.

## Model Interpretation

A key advantage of the proposed Zero-Inflated Poisson (ZIP) framework is its inherent interpretability. By decomposing the counting process into distinct probabilistic components, ZIP enables us to diagnose the model’s behavior by separately analyzing where it focuses and how much it counts, as illustrated in Fig. 10.

The structural zero map ( $\pi$ ) functions as a learned attention or segmentation mechanism. This branch estimates the probability that a given block is structurally irrelevant to crowd counting (e.g., background, buildings, torso, or peripheral head parts) and should be suppressed. As shown in Fig. 10b, the model assigns high structural-zero probability (deep red) to background areas like pavement, while assigning low probability (blue/cyan) to compact regions containing head centers. Note that this spatial disentanglement is learned without any segmentation supervision, showing that ZIP can implicitly separate relevant and irrelevant regions using only point-level annotations.

In parallel, the lambda map  $\lambda$  captures the expected count per block. As visualized in Fig. 10c, high values appear in the upper part of the image where the crowd is denser due to perspective.

The sampling zero map (Fig. 10d) models the probability that a block receives a zero count due to sampling effects (*i.e.*, head-center blocks receive a zero counts because of the point-based annotation). It is computed as  $(1 - \pi) \otimes \exp(-\lambda)$ , and is highest where the model is confident a person is present (low  $\pi$ ), but the predicted count is modest (moderate  $\lambda$ ).

The complete zero probability map (Fig. 10e) represents the overall likelihood that a block receives a zero count from any source (either structural or sampling). It is defined as  $\pi + (1 - \pi) \otimes \exp(-\lambda)$ . This map is often dominated by the structural zero component, as the background makes up the majority of the image. It can be viewed as an inverse attention map, where non-red regions highlight areas the model expects to contain people.

Finally, the predicted density map  $\mathbf{Y}^*$  (Fig. 10f) is computed as  $(1 - \pi) \otimes \lambda$ , combining spatial suppression and count estimation. This yields a clean and well-localized density prediction, with high activations concentrated near annotated head centers.

Together, these components demonstrate how ZIP not only improves counting accuracy, but also offers fine-grained interpretability by isolating both spatial relevance and count magnitude across the image.

### Additional Qualitative Visualizations

We curate ten images from the validation split of NWPU-Crowd to demonstrate the qualitative behavior of ZIP-B in five representative scenes (two images per scene). For clarity we organize the examples into a regular group (background-only, sparse, and crowded) and a challenging group (multi-scale and low-illumination). The results are shown in Fig. 11 and Fig. 12, respectively.

**Background-only (Fig. 11a).** The structural-zero branch assigns a uniformly high zero-probability to every pixel, and the density branch outputs all-zero maps, matching the ground-truth counts of 0.

**Sparse (Fig. 11b).** With only a handful of pedestrians, the structural-zero map suppresses the background while isolating small blue blobs around true head centers; the resulting density maps reproduce the exact person counts.

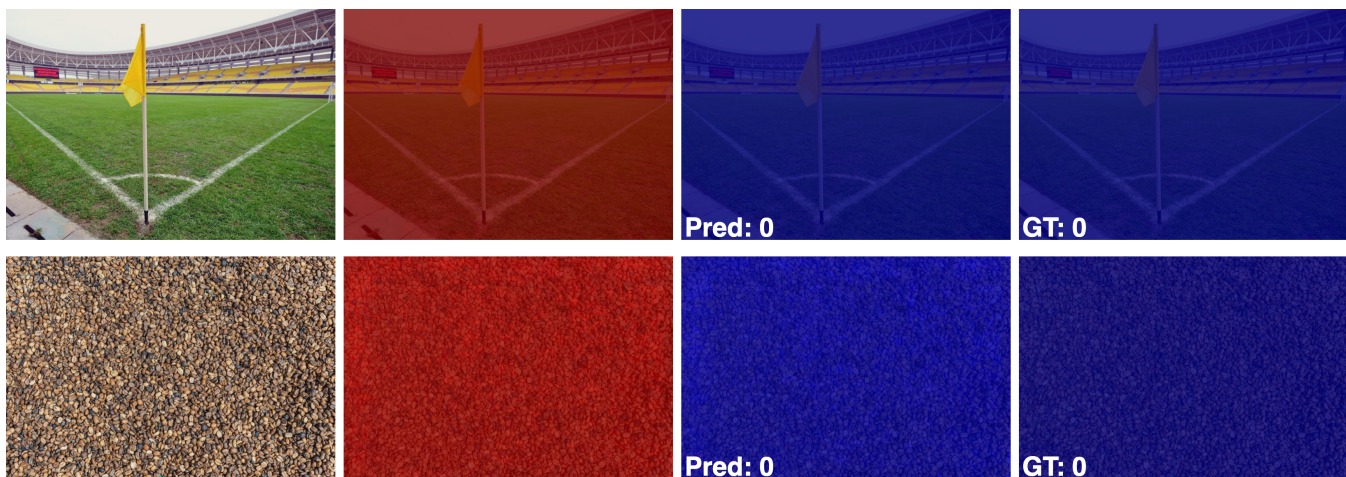
**Crowded (Fig. 11c).** In the two stadium-like scenes containing several thousand people, the model still produces a clean, high-resolution density map. The total count deviates from ground truth by less than 0.5%, confirming that ZIP modeling scales to extreme densities.

**Multi-scale (Fig. 12a).** The foreground heads are large and the background heads extremely small. The structural-zero map adapts its granularity: it keeps broad foreground regions non-zero while aggressively filtering distant background pixels, enabling accurate detection across scales.

**Low-illumination (Fig. 12b).** Despite poor lighting, the structural-zero branch reliably removes dark background regions, allowing the density branch to localize heads and deliver a near-exact total count.

Together, these qualitative results show that the explicit modeling of structural zeros enables ZIP-B to generalize from empty backgrounds to dim, highly congested, and multi-scale scenes without any segmentation supervision.

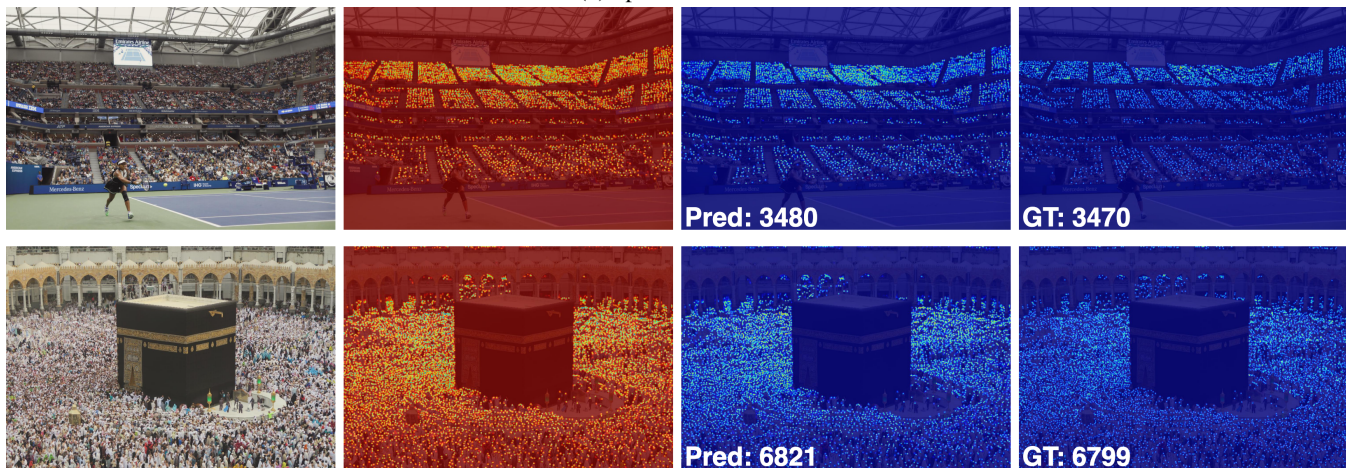




(a) Background-only instances.



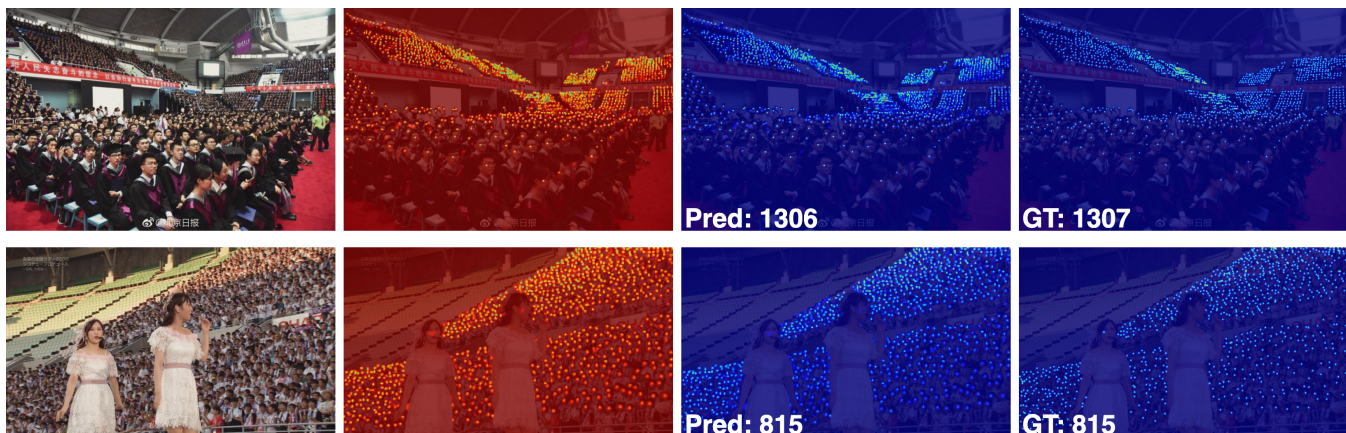
(b) Sparse scenarios.



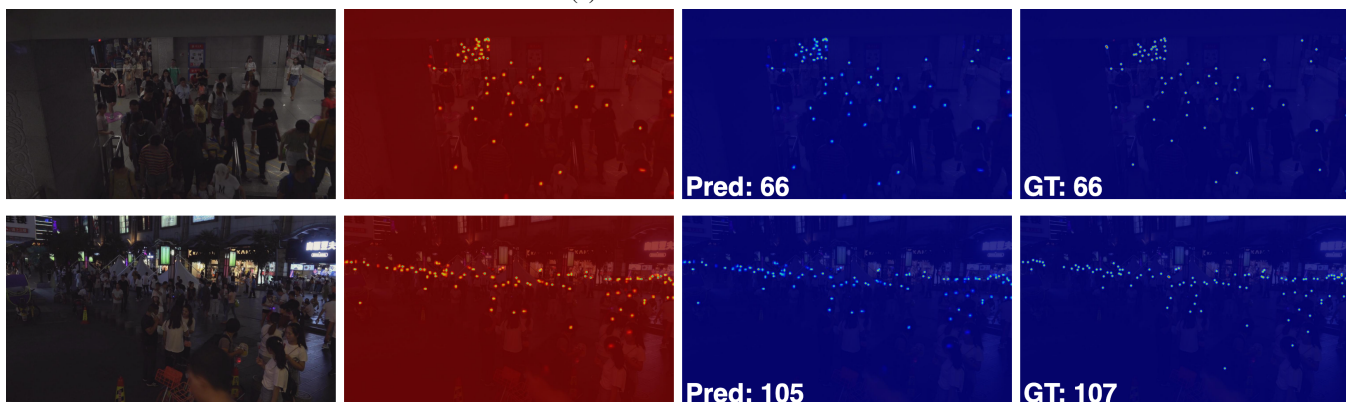
(c) Highly crowded scenarios.

Figure 11: Visualized results on background-only, sparse and highly congested scenes in NWPU-Crowd (predictions by ZIP-B). Each row shows, from left to right, the input image, the predicted structural-zero map, the predicted density map, and the ground-truth density map. In the background-only examples (Fig. 11a), the structural-zero branch correctly classifies the entire image as background, yielding an all-zero density map. In the sparse cases (Fig. 11b), ZIP-B still localizes every head and reproduces the exact crowd count. As for the highly crowded scenes (Fig. 11c), ZIP-B can still produce accurate density maps and counts.





(a) Multi-scale scenes.



(b) Low-illumination examples.

Figure 12: Qualitative results on two challenging scenarios in NWPU-Crowd (predictions by ZIP-B): multi-scale (Fig. 12a) and low-illumination (Fig. 12b). For each row, the columns show (1) input image, (2) predicted structural-zero map, (3) predicted density map, and (4) ground-truth density map. In the multi-scale examples (Fig. 12a), the scenes contain a large variety of head sizes, ranging from large, close-up people to tiny, distant heads; ZIP-B suppresses background pixels while simultaneously detecting heads at all scales, yielding an accurate total count. In the low-illumination examples (Fig. 12b), the structural-zero branch can still filter the background, enabling the density branch to produce a clean, well-localized prediction despite poor lighting.